200236-F

ASSIMILATION OF SAR IMAGERY IN A NEARSHORE SPECTRAL WAVE MODEL

Prepared for: OFFICE OF NAVAL RESEARCH
875 North Randolph Street, Suite 1425
Arlington, Virginia 22203-1995

By: David T. Walker
General Dynamics Advanced Information Systems
1200 Joe Hall Drive
Ypsilanti, MI 48197

Final Report

Contract Number: N00014-03-C-0164

DISTRIBUTION STATEMENT A
Approved for Public Release
Distribution Unlimited

Date: March 2006

GENERAL DYNAMICS
Advanced Information Systems

REPORT DOCUMENTATION PAGE	*Form Approved* **OMB No. 0704-0188**

1. REPORT DATE *(DD-MM-YYYY)* 03-15-2006	**2. REPORT TYPE** Final	**3. DATES COVERED** *(From - To)* 06 March 2003 - 31 December 2005

4. TITLE AND SUBTITLE ASSIMILATION OF SAR IMAGERY IN A NEARSHORE SPECTRAL WAVE MODEL	**5a. CONTRACT NUMBER** N00014-03-C-0164
	5b. GRANT NUMBER
	5c. PROGRAM ELEMENT NUMBER
6. AUTHOR(S) David T. Walker General Dynamics Advanced Information Systems 1200 Joe Hall Drive Ypsilanti, MI 48197	**5d. PROJECT NUMBER** 200236
	5e. TASK NUMBER
	5f. WORK UNIT NUMBER
7. PERFORMING ORGANIZATION NAME(S) AND ADDRESS(ES) General Dynamics–Advanced Information Systems	**8. PERFORMING ORGANIZATION REPORT NUMBER** 200236-F
9. SPONSORING/MONITORING AGENCY NAME(S) AND ADDRESS(ES) Office of Naval Research 875 North Randolph Street, Suite 1425 Arlington, Virginia 22203-1995	**10. SPONSOR/MONITOR'S ACRONYM(S)** ONR
	11. SPONSORING/MONITORING AGENCY REPORT NUMBER

12. DISTRIBUTION AVAILABILITY STATEMENT
Approved for Public Release: Distribution Unlimited

13. SUPPLEMENTARY NOTES

14. ABSTRACT

This report describes a variational-calculus-based methodology for assimilation of data into a near-shore spectral wave model. Application of the methodology to both in-situ and SAR-image data are described. The use of the assimilation procedure to estimate both the wave field and the bottom friction coefficient are demonstrated for the region near the USACE Field Research Facility in Duck NC. Results for assimilation of in-situ data show good agreement with independent wave spectrum observations. Assimilation of SAR-image data yields good agreement also; however, wave energy at high frequencies and large propagation angles relative to the SAR look direction is lost. This is due to well-known SAR-imaging effects. Results for estimation of the bottom-friciton coefficient using SAR imagery indicate that this is feasible, but additional development work is required.

15. SUBJECT TERMS
Inverse modeling, wave modeling, data assimilation, synthetic aperture radar.

16. SECURITY CLASSIFICATION OF:			**17. LIMITATION OF ABSTRACT** SAR	**18. NUMBER OF PAGES** 33	**19a. NAME OF RESPONSIBLE PERSON** David T. Walker
a. REPORT U	**b. ABSTRACT** U	**c. THIS PAGE** U			**19b. TELEPONE NUMBER** ***(Include area code)*** (734)480-5416

Abstract

This report describes a variational approach for assimilation of data into a near-shore spectral wave model. Application of the methodology to both in-situ and SAR-image data are described. The use of the assimilation procedure to estimate both the wave field and the bottom friction coefficient are demonstrated for the region near the USACE Field Research Facility in Duck NC. Results for assimilation of in-situ data show good agreement with independent wave spectrum observations. Assimilation of SAR-image data yields good agreement also; however, wave energy at high frequencies and large propagation angles relative to the SAR look direction is lost. This is due to well-known SAR-imaging effects. Results for estimation of the bottom-friction coefficient using SAR imagery indicate that this is feasible, but additional development work is required.

Contents

Page

List of Figures

1 Introduction

Mature and accurate computational models exist for many oceanographic applications; however, the required model inputs, in particular boundary condition data, are not directly available in many cases of practical interest. The data that does exist tends to be at the wrong locations, interior to the spatial domain of interest and not on the boundary. This incompatibility between the required model inputs and the available data represents a significant obstacle to using observational data to improve model predictions.

In this study the use of observational data in model calculations of the wave spectrum in the near-shore region is examined. The model used is the SWAN model [18, 4], a near-shore wave-spectrum model, which implements conservation of the wave-action spectral density in shallow water. The model can include the effects of variable bathymetry, currents, bottom friction, depth-induced breaking, wind input and whitecapping. The problem to be examined is the use of observations at interior points in the region of interest to estimate the appropriate incident-wave spectrum boundary conditions and/or the bottom friction coefficient under steady-state conditions.

The observational data to be examined will include satellite-based SAR imagery, as well as in-situ observations of the wave directional spectrum. For SAR data assimilation, a fully nonlinear mapping approach [10, 12] is used to estimate the SAR-image spectrum from the wave spectrum. In the mapping from the wave spectrum to the SAR image, some of the wave information in lost; energy at high wavenumbers in general, and at high azimuth wave numbers, in particular, is lost. This effect will be apparent in some of the results.

The variational approach adopted here follows that of Bennett [2] in its derivation, and that of LeDimet & Talagrand [14] in application. An objective function is defined which quantifies the error in the model prediction of the observation data. To ensure the uniqueness of the result, the cost function includes a term which 'penalizes' the estimated model inputs [3]. An adjoint SWAN model equation is derived which has as an input the difference between the model prediction and the observation data. From the adjoint solution the gradient of the objective function with respect to the model inputs, the incident wave spectrum and/or the bottom friction coefficient are calculated. The gradient is used together with a conjugate-gradient minimization algorithm to determine the model inputs which minimize the objective function.

In the next section, the SWAN model and the SAR-image spectrum model is described. Then the objective function is defined and the adjoint SWAN model is derived, along with expressions for the gradient of the cost function with respect to the model inputs. After that, the algorithm is applied to synthetic data and real-world data: both in-situ spectrum measurements and SAR-image data. In the real-world data cases, the results for the estimated wave field are evaluated by comparison to independent data.

2 The Models

The assimilation procedure relies on two models, one which governs the wave spectrum and another which relates the wave spectrum to the spectrum of the SAR image.

2.1 The Wave Spectrum Model

The SWAN model [18, 4] is a near-shore wave-action-balance model which can predict the evolution of the wave spectrum in coastal regions. The wave-action spectral balance is expressed as

$$\frac{\partial N}{\partial t} + \widetilde{\nabla} \cdot (\widetilde{\mathbf{C}} N) = \frac{S(N)}{\sigma}, \tag{1}$$

where x and y are spatial position variables, and σ and θ are wave frequency and direction variables for the action spectrum, $\widetilde{\nabla} = (\frac{\partial}{\partial x}, \frac{\partial}{\partial y}, \frac{\partial}{\partial \sigma}, \frac{\partial}{\partial \theta})$, and $\widetilde{\mathbf{C}} = (C_x, C_y, C_\sigma, C_\theta)$ represents the wave-energy propagation velocities in physical and spectral space. Below, the vectors $\mathbf{x} = (x, y)$ and $\mathbf{s} = (\sigma, \theta)$ will be used to represent spatial and spectral position, respectively. $N(\mathbf{x}, \mathbf{s}, t)$ is the action spectral density defined as

$$N(\mathbf{x}, \mathbf{s}, t) = E(\mathbf{x}, \mathbf{s}, t)/\sigma, \tag{2}$$

where E is the energy spectral density and

$$\sigma(k) = \sqrt{gk \tanh kh}. \tag{3}$$

is the intrinsic radian frequency, where g is the gravitational acceleration, $h(\mathbf{x})$ is the water depth, and $k = 2\pi/\lambda$ is the wavenumber (λ is the wave length). The $x-$ and $y-$direction components of the wave-propagation velocities are given by

$$C_x = U + C_g \cos\theta, \qquad C_y = V + C_g \sin\theta, \tag{4}$$

where $U(\mathbf{x}, t)$ and $V(\mathbf{x}, t)$ are the x and y direction current velocities, specified as inputs to the problem, and the wave group velocity is

$$C_g = \frac{1}{2}\sqrt{\frac{g}{k} \tanh kh}\left(1 + \frac{2kh}{\sinh 2kh}\right). \tag{5}$$

The other two velocities C_σ and C_θ are energy propagation velocities in the spectral domain caused by depth and current variations. They are most easily defined in terms of the apparent frequency Ω (as seen by a stationary observer), which includes a doppler shift induced by the current

$$\Omega = \sigma + k\left(U \cos\theta + V \sin\theta\right). \tag{6}$$

The spectral propagation velocities are given by

$$C_\sigma = \frac{\partial \Omega}{\partial t}, \qquad C_\theta = \frac{1}{k}\left(\frac{\partial \Omega}{\partial x} \sin\theta + \frac{\partial \Omega}{\partial y} \cos\theta\right). \tag{7}$$

The source term on the right-hand side of (1) is described in detail in [18] and includes the effects of wind growth and energy transfer in the spectrum due nonlinear wave-wave interactions (resonant triad and quartet interactions). Significant additional contributors to the source term are various processes by which wave energy is dissipated. These include whitecapping, bottom friction and depth-induced breaking. Energy loss due to whitecapping is dependent on wave steepness and is parameterized following the pulse-based model of [8], adapted by WAMDI Group (1988),

$$S_{d,w} = -\Gamma \; \tilde{\sigma} \frac{k}{\tilde{k}} \; E, \tag{8}$$

where $\tilde{\sigma}$ is the mean intrinsic frequency and $\tilde{k}$ is the mean wavenumber. Γ is a steepness-dependent coefficient estimated by examining fully developed conditions. The general form of the bottom friction source term is

$$S_{d,b} = -C_b \; \frac{\sigma^2}{g^2 \sinh^2 kh} \; E = -C_b \; f(\sigma, h) \; E, \tag{9}$$

where C_b is a spatially varying dissipation coefficient that can be parameterized as a function of the bottom roughness, integral spectral parameters, or the frequency and direction of a wave component (see [8], [9], [5], [15]). For depth-induced breaking, SWAN essentially preserves the spectral shape (dissipates the spectrum uniformly) and uses the simple saturated breaker criterion with an allowed variability for bottom slope

$$S_{d,br} = -\frac{S_{d,br,tot}}{E_{tot}} \; E, \tag{10}$$

where $S_{d,br.tot}$ is the rate of total wave energy dissipation and is determined following Battjes and Janssen (1978).

This set of equations can be solved for the action spectrum for spatial region $\mathcal{R}$ subject to appropriate boundary conditions on $\partial\mathcal{R}$. For portions of the wave spectrum with propagation velocities which carry energy into $\mathcal{R}$, the 'incident' wave spectrum $N(\mathbf{x}, \mathbf{s}, t)$ on the boundary $\partial\mathcal{R}$ must be specified; for the portions of the wave spectrum for which the propagation velocities carry the energy outward from $\mathcal{R}$, an 'outflow' condition is used (continuity of the action flux at $\partial\mathcal{R}$). In the spectral domain, for most practical implementations, the spectral density is required to vanish on the upper and lower frequency (σ) boundaries; this condition is satisfied by locating the σ boundary far from the energy-containing region of the spectrum. The boundary conditions in θ are that the spectrum is periodic. In addition to these boundary and initial conditions, complete specification of the mathematical problem requires the the bathymetry $h(\mathbf{x})$ and current field $U(\mathbf{x}, t)$, $V(\mathbf{x}, t)$ to be prescribed for spatial region $\mathcal{R}$.

2.2 The SAR-Image Spectrum Model

The SAR -image spectrum can be related to the wave spectrum through either a fully nonlinear mapping, or a less-accurate but simpler, quasi-linear model. These are described in the next sections.

Nonlinear SAR Model

A model which relates the SAR-image spectrum to the ocean-wave spectrum has been derived by Hasselmann & Hasselmann [10] and Krogstad [12]. As summarized by Lyzenga [13], the SAR-image spectrum is given by

$$I(\mathbf{k}) = \frac{1}{4\pi^2} \int\int G(\mathbf{r}, k_a) e^{-i\mathbf{k}\cdot\mathbf{r}} d\mathbf{r} \tag{11}$$

where $\mathbf{r}$ is a position vector in correlation space, k_a is the azimuth (along-track) wavenumber component of $\mathbf{k}$, the wave vector. The term in the integrand is defined as

$$G(\mathbf{r}, k_a) = \left[\rho_{rr}(\mathbf{r}) + f(\mathbf{r}, k_a) f(-\mathbf{r}, -k_a)\right] e^{-k_a^2 C(\mathbf{r})}, \tag{12}$$

where

$$f(\mathbf{r}, k_a) = 1 - ik_a \left[\rho_{rv}(0) - \rho_{rv}(\mathbf{r})\right], \tag{13}$$

$$C(\mathbf{r}) = \rho_{vv}(0) - \rho_{vv}(\mathbf{r}), \tag{14}$$

and the spatial correlation functions ρ_{rr} and ρ_{vv}, as well as the cross-correlation function ρ_{rv}, are defined as

$$\rho_{rr}(\mathbf{r}) = \int\int |T_r(\mathbf{k})|^2 E(\mathbf{k}) e^{i\mathbf{k}\cdot\mathbf{r}} d\mathbf{k}, \tag{15}$$

$$\rho_{vv}(\mathbf{r}) = \int\int |T_v(\mathbf{k})|^2 E(\mathbf{k}) e^{i\mathbf{k}\cdot\mathbf{r}} d\mathbf{k}, \text{ and} \tag{16}$$

$$\rho_{rv}(\mathbf{r}) = \int\int T_r(\mathbf{k})\, T_v^*(\mathbf{k}) E(\mathbf{k}) e^{i\mathbf{k}\cdot\mathbf{r}} d\mathbf{k}. \tag{17}$$

Here,

$$T_v(\mathbf{k}) = \frac{R}{\sigma V} \left(gk_r \sin\theta_i - i\sigma^2 \cos\theta_i\right), \tag{18}$$

where R is the range from the sensor to the scene center, V is the sensor velocity, σ is the wave frequency from (3), k_r is the range (cross-track) component of $\mathbf{k}$ and θ_i is the incidence angle. The other function is given by

$$T_r(\mathbf{k}) = k\left[m_h(\mathbf{k}) + i m_t(\mathbf{k})\right], \tag{19}$$

where $k = |\mathbf{k}|$. The 'hydrodynamic' modulation of the radar reflectivity is given by

$$m_h(\mathbf{k}) = \frac{m_0}{\tanh kh} \sqrt{\frac{g}{U\sigma}} \cos^2(\theta - \theta_r), \tag{20}$$

where θ_r is the radar look direction and θ is the wave propagation direction; $m_0 = 7.5$ for vertical polarization and $m_0 = 12.5$ for horizontal polarization. The 'tilt' modulation is given by

$$m_t(\mathbf{k}) = (5\cot\theta_i + 4\tan\theta_i - 4\,\gamma_p\, \sin\theta_i)\cos(\theta - \theta_r), \tag{21}$$

with

$$\begin{aligned} \gamma_p &= \frac{1}{\cos\theta_i + n} && \text{for horizontal polarization,} \\ &= \frac{n}{n\cos\theta_i + 1} + \frac{\cos\theta_i}{1+\sin^2\theta_i} && \text{for vertical polarization,} \end{aligned} \tag{22}$$

and for sea water $n \approx 9$.

Quasi-Linear SAR Model

As is evidenced by (11) through (22), the full nonlinear mapping between the ocean-wave spectrum E and the SAR-image spectrum I is quite complicated. A simpler, quasi-linear approximation [10] can be expressed as

$$I(\mathbf{k}) \approx M'_S(\mathbf{k})\ E(\mathbf{k}) + M'_S(-\mathbf{k})\ E(-\mathbf{k}) \tag{23}$$

where

$$M'_S(\mathbf{k}) = \frac{1}{2}\left|T_r(\mathbf{k}) + ik_a T_v(\mathbf{k})\right|^2 e^{-k_a^2\sigma_v^2} \tag{24}$$

where $T_r(\mathbf{k})$ and $T_v(\mathbf{k})$ are as specified above, and $\sigma_v^2 = \rho_{vv}(0)$. For use in the assimilation procedure, this can be re-written in polar $\mathbf{s} = (\sigma, \theta)$ coordinates as

$$I(\mathbf{s}) = M_S(\mathbf{s})\ E(\mathbf{s}) + M_S(\mathbf{s}^-)\ E(\mathbf{s}^-), \tag{25}$$

where $\mathbf{s}^- = (\sigma, \theta - \pi)$ and

$$M_S(\mathbf{s}) = k\frac{dk}{d\sigma} M'_S(\mathbf{k}). \tag{26}$$

For the results shown herein, the full Hasselmann & Hasselmann model (11–22) was used for forward prediction of the SAR-image spectrum, while the adjoint SAR model used in the inversion procedure was based on the quasi-linear model shown in (24).

3 Assimilation Methodology

In this section the basis for the variational data assimilation approach is developed. The problem setup will follow the 'weak constraint' formulation of Bennett [2], but the strong constraint limit will be taken, yielding an approach similar to that of Le Dimet & Talagrand [14]. The model inputs being estimated are penalized in the objective function to ensure uniqueness [3]. An objective function is defined which is a positive-definite measure of the difference between a set of observations and the model predictions, as well as the fit of the models to the data. This objective function is to be minimized by adjusting the SWAN-model inputs. For the purposes of this study, only stationary conditions will be considered, and the model inputs are taken to be the boundary conditions (incident-wave spectra) and the bottom friction coefficient.

In what follows, we first define the objective function to be minimized (J). We then determine the conditions for a minimum in J, the Euler–Lagrange equations. This is followed by the relations, deriver from the Euler–Lagrange equations used in the assimilation algorithm. The section closes with the steps implemented in the assimilation algorithm.

3.1 The Objective Function

Our goal is to minimize the error in our prediction of some observable quantity $D(\mathbf{x}, \mathbf{s})$ compared to a set of observations. The observation data D are taken to be related to the wave energy spectrum E by

$$D(\mathbf{x}, \mathbf{s}) = M(\mathbf{s})E(\mathbf{x}, \mathbf{s}) + M(\mathbf{s}^-)E(\mathbf{x}, \mathbf{s}^-), = ME + (ME)^-, \tag{27}$$

where $M(\mathbf{x}, \mathbf{s})$ is in this case a transfer function. For direct observations of the wave spectrum, $M = 1$ and $(ME)^- = 0$, while for SAR observations, $M = M_S$ from (24), above. For a set of N_d observations at spatial locations $\mathbf{x}_i$, the error variance between the predictions and observations can be expressed as

$$\frac{1}{N_d} \sum_{i=1}^{N_d} \int_{\mathcal{R}} \int_{S} (D - \widehat{D_i})^2 \delta_{\mathbf{x}_i} \, d\mathbf{s} \, d\mathbf{x},$$

where $\widehat{D_i}$ is an observation of D at location $\mathbf{x}_i$, $\delta_{\mathbf{x}_i} = \delta(\mathbf{x} - \mathbf{x}_i)$ is a function sampling D at $\mathbf{x}_i$ for comparison to the data, and the integral is over the entire spectrum.

To obtain a prediction from our coupled wave-spectrum/SAR-spectrum model which matches a set of observations, we first define an objective function to be minimized, which includes both the data and the models used to predict the data, along with any additional constraints to be placed on the solution. In this approach, we wish to minimize the error in the predictions of the observed data, as well as the misfit between the models and the actual physics. The objective function J is

$$\begin{aligned} J &= \frac{1}{2} \int_{\mathcal{R}} \int_{S} \sum_{i=1}^{N_d} (D - \widehat{D_i})^2 \delta_{\mathbf{x}_i} \, d\mathbf{s} \, d\mathbf{x} \\ &+ \frac{1}{2} \int_{\mathcal{R}} \int_{S} w \left\{ \sum_{i=1}^{N_d} \left[D - ME - (ME)^- \right]^2 \delta_{\mathbf{x}_i} \right. \\ &\qquad\qquad \left. + \frac{\phi_m}{A_r} \left[\widetilde{\nabla} \cdot \left(\widetilde{\mathbf{C}} N \right) + C_b f \frac{E}{\sigma} \right]^2 \right\} d\mathbf{s} \, d\mathbf{x} \\ &+ \frac{1}{2} \int_{\mathcal{B}} \int_{S} w_b \frac{\phi_m}{L_b} \, E^2 \, d\mathbf{s} \, d\mathbf{x}_b + \frac{1}{2} \int_{\mathcal{R}} \int_{S} w_f \frac{\phi_f}{A_r \sigma^2} \left(C_b \, f \right)^2 d\mathbf{s} \, d\mathbf{x} \, , \end{aligned} \tag{28}$$

where the first line is recognized as proportional to the error variance between the model and the data, the second and third contain the mean-square misfit of the models for the SAR spectrum and the wave spectrum. The last line contains positive-definite measures of the model inputs to be estimated, the boundary spectrum $E(\mathbf{x}_b, \mathbf{s})$, and the spatially varying bottom friction coefficient C_b; these are included to ensure a unique solution [3]. In (28), A_r is the area of the spatial domain, ϕ_m is a constant with the same units as M^2, L_b is the length of the boundary, x_b is the position along the boundary, and ϕ_f is a constant with the same units as D. Here w is a weighting factor controlling the contribution of the model misfit to the objective function, relative to the data, and w_b and w_f are weighting factors controlling the contributions of the estimated model inputs.

3.2 The Euler–Lagrange Equations

The objective function J depends on D, E, C_b and the models that relate them. The best fit of the model results to the data will be for the boundary spectrum and bottom friction coefficient which makes J stationary, i.e. when the first variation of J with respect to these variables vanishes. The first variation of (28) with respect to D, E and C_b has three components

$$\delta J = \delta J_D + \delta J_E + \delta J_{C_b}. \tag{29}$$

The relations which define the minimum, which are satisfied when δJ_D, δJ_E, and δJ_{C_b} vanish are the Euler–Lagrange equations.

The first component of δJ is given by

$$\delta J_D = \int_{\mathcal{R}} \int_{\mathcal{S}} \sum_{i=1}^{N_d} \left\{ (D - \widehat{D}_i) + w[D - ME - (ME)^-] \right\} \delta_{\mathbf{x}_i} \, \delta D \, d\mathbf{s} \, d\mathbf{x}, \tag{30}$$

Since the region over which the integration occurs is essentially arbitrary, and δD is in general non-zero, δJ_D will vanish when

$$\sum_{i=1}^{N_d} \left[D - ME - (ME)^- \right] \delta_{\mathbf{x}_i} = - \sum_{i=1}^{N_d} \frac{1}{w} \left(D - \widehat{D}_i \right) \delta_{\mathbf{x}_i}. \tag{31}$$

The second component of δJ is, after integration by parts,

$$\begin{aligned} \delta J_E \quad = \quad & - \int_{\mathcal{R}} \int_{\mathcal{S}} \left\{ w \sum_{i=1}^{N_d} \left[D - ME - (ME)^- \right] M \delta_{\mathbf{x}_i} + \left[\widetilde{\mathbf{C}} \cdot \widetilde{\nabla} A - C_b f A \right] \right\} \delta E \, d\mathbf{s} \, d\mathbf{x} \\ & + \int_{\mathcal{B}} \int_{\mathcal{S}} \left(w_b \frac{\phi_m}{L_b} E + A \widetilde{\mathbf{C}} \cdot \mathbf{n} \right) \delta E \, d\mathbf{s} \, d\mathbf{x}_b, \end{aligned} \tag{32}$$

where $\mathbf{n}$ is a unit vector normal to the domain boundary, and

$$A = \frac{w \phi_m}{A_r \sigma} \left[\widetilde{\nabla} \cdot \left(\widetilde{\mathbf{C}} N \right) + C_b f \frac{E}{\sigma} \right]. \tag{33}$$

Both integrals in (32) will vanish independently at the minimum for J. Requiring the first, area, integral to be zero yields

$$\tilde{\mathbf{C}} \cdot \widetilde{\nabla} A = C_b f A - w \sum_{i=1}^{N_d} \left[D - ME - (ME)^{-} \right] M \delta_{\mathbf{x}_i}. \tag{34}$$

and (32) becomes

$$\delta J_E \;=\; \int_{\mathcal{B}} \int_S \left(w_b \frac{\phi_m}{L_b} E + A \tilde{\mathbf{C}} \cdot \mathbf{n} \right) \delta E \, d\mathbf{s} \, d\mathbf{x}_b, \tag{35}$$

where only the integral along the boundary is retained. The final component of δJ is

$$\delta J_{C_b} = - \int_{\mathcal{R}} \int_S \left(f A E - w_f \frac{\phi_f f^2}{A_r \sigma^2} C_b \right) \delta C_b \, d\mathbf{s} \, d\mathbf{x} \ . \tag{36}$$

At the minimum in J we must have then

$$0 \;=\; \int_{\mathcal{B}} \int_S \left(w_b \frac{\phi_m}{L_b} E + A \tilde{\mathbf{C}} \cdot \mathbf{n} \right) \delta E \, d\mathbf{s} \, d\mathbf{x}_b \tag{37}$$

and

$$0 = - \int_{\mathcal{R}} \int_S \left(f A E - w_f \frac{\phi_f f^2}{A_r \sigma^2} C_b \right) \delta C_b \, d\mathbf{s} \, d\mathbf{x} \ . \tag{38}$$

The Euler–Lagrange equations, those which define the minimum for J, are (31), (34), (37) and (38), along with definition (33).

3.3 The Assimilation Equations

The assimilation procedure is intended to find the model inputs E_b and C_b which results in a solution $E(\mathbf{x}, \mathbf{s})$ that satisfies the Euler–Lagrange equations. The equations used in the assimilation procedure include the governing equation for $E(\mathbf{x}, \mathbf{s})$,

$$\widetilde{\nabla} \cdot \left(\tilde{\mathbf{C}} \, \frac{E}{\sigma} \right) = -C_b f \frac{E}{\sigma} + \frac{A_r \sigma}{w \phi_m} A, \tag{39}$$

and the 'adjoint' equation governing $A(\mathbf{x}, \mathbf{s})$ which results from combining (31) and (34),

$$\tilde{\mathbf{C}} \cdot \widetilde{\nabla} A = C_b f A + \sum_{i=1}^{N_d} M \left(D - \widehat{D}_i \right) \delta_{\mathbf{x}_i}. \tag{40}$$

The adjoint equation includes the model–data error, and the transfer function M from the sensor model (27), on the right-hand side. To obtain expressions for the gradient of J with respect to the model inputs, we use (35), which leads to

$$\frac{\partial J}{\partial E_b} = \phi_m w_b E_b + \int_{\mathcal{B}} A \tilde{\mathbf{C}} \cdot \mathbf{n} \, d\mathbf{x}_b, \tag{41}$$

for a boundary spectrum which is constant in space, $E(\mathbf{x}_b, \mathbf{s}) = E_b(\mathbf{s})$, and (36), which leads to

$$\frac{\partial J}{\partial C_b} = \int_S \left(w_f \frac{\phi_f f^2}{A_r \sigma^2} C_b - f A E \right) d\mathbf{s}. \tag{42}$$

At the minimum for the objective function J, these gradients will be zero, thereby satisfying the Euler–Lagarange equations.

Equations (39) through (42), along with the sensor model (27), constitute the full set of equations for our data assimilation problem. This is a weak constraint formulation, where the governing SWAN model and the sensor model are not required to be exactly satisfied. As a result, (39) and (40) are coupled through forcing terms on their right-hand sides, and require a simultaneous solution. These equations can be uncoupled by allowing $w \rightarrow \infty$, which causes (39) to revert back to (33). This results in the 'strong constraint' formulation, where the forward models are taken as exact, and all the error is assumed to reside in the data.

3.4 The Assimilation Algorithm

For the results presented below, wave-spectrum or SAR-image-spectrum observations at one or more points are used.The initial guess for the wave spectrum over the entire region is zero, including the incident wave spectrum. The adjoint equation (40) is solved with the observations as input, and the adjoint solution is used to calculate the gradient (41), (42). The gradient is used in a conjugate-gradient procedure [16] to find the incident wave spectrum and bottom friction coefficient which results in the minimum in the cost function J. In practice, the following sequence of steps is followed:

1. The adjoint solution is calculated using using the error in the most recent prediction as input (i.e. the second term on the right-hand side of equation 40).
2. From the adjoint solution, the gradient is determined using (41), (42).
3. The conjugate gradient algorithm is used to calculate a new estimate of the incident wave spectrum E_b and/or bottom friction C_b.
4. The SWAN model is run with the new inputs and a new wave-spectrum prediction for the region is generated.
5. The sensor model is run with the new spectrum as input and a new prediction of the data is generated. For SAR-image data, the sensor model is the Hasselmann & Hasselmann fully nonlinear model (11), while for in-situ data the sensor model is a unit transfer function.

These steps are repeated until the gradient of J goes to zero, which occurs when the cost function ceases to change. The final prediction from the SWAN model is considered the 'best-fit' to the observation data.

4 Application of the Assimilation Algorithm

Here we apply the assimilation algorithm three ways: First we apply it to in-situ wave-spectrum observations to estimate the incident wave spectrum which yields a prediction matching the observations. This is done first for synthetic observations (generated using the SWAN model), and then for actual field data. The algorithm is then applied to SAR-image data, again being used to estimate the incident wave spectrum for first simulated SAR-image spectra and then for actual ERS SAR-image spectra. Finally, initial results showing estimation of bottom friction from ERS SAR data is presented.

The assimilation procedure will be applied for a region off the Atlantic coast, centered on the US Army Corps of Engineers Field Research Facility (FRF) in Duck, NC. The bathymetery for the region is shown in figure 1 and extends 277.8 km North–South. from South of Cape Hatteras to North of the mouth of the Chesapeake Bay, and 134.4 km East–West. so that it extends offshore beyond the continental shelf. For the cases examined below, the region shown in figure 1 is discretized at 995 m (E-W) and 2013 m (N-S) resulting in a 136 × 139 computational grid. The origin of the coordinate system, the lower. left-hand corner of the region in figure 1. is located at 35°N 76°W. and it extends from $35^\circ - 36.5^\circ$N and $76^\circ - 74.5^\circ$W. The wave spectrum has 25 frequencies logarithmically spaced from 0.042–0.411 Hz. and 48 equally spaced directions covering 360°. A spatially uniform wave spectrum at the Eastern incident-wave boundary is considered and so it is desirable that the Eastern boundary be in uniformly 'deep' water (i.e. that none of the waves are influenced by the bottom). It is assumed that no waves enter at the North and South boundaries. At the shore boundary. the action spectral density vanishes. Due to the lack of waves on the North and South boundaries. the solution will not be valid in triangular regions which grow Westward from the Eastern corners of the domain. The region chosen will therefore allow a portion of the coastline roughly 100–150 km in extent to be accurately simulated with the specification of a constant incident wave spectrum.

In practice. the SWAN model (v40.11) is used for the forward predictions of the wave spectrum. A modified version of the SWAN model (v30.75) is used to solve the adjoint equations. The calculation of the cost function and the observation term for the adjoint equations is done using a separate FORTRAN code. The conjugate gradient minimization algorithm and calculation of the incident wave spectrum are implemented in yet another FORTRAN code. The iteration scheme outlined above is carried out by executing the various codes under control of a C-shell script. For the SWAN model predictions, depth-induced wave breaking and bottom friction are included, but not wind growth, white-capping or nonlinear interactions. For the adjoint SWAN solutions, all source terms are ignored in order to simplify the implementation of the adjoint.

4.1 Estimation of the Wave Field from In-Situ Observations

Application to Simulated Wave-Spectrum Data

In order to assess the accuracy of the assimilation procedure, it will be applied initially to a synthetic data set, generated by a forward run of the SWAN model. Use of synthetic data allows the procedure to be evaluated independent of the accuracy of the SWAN model itself.

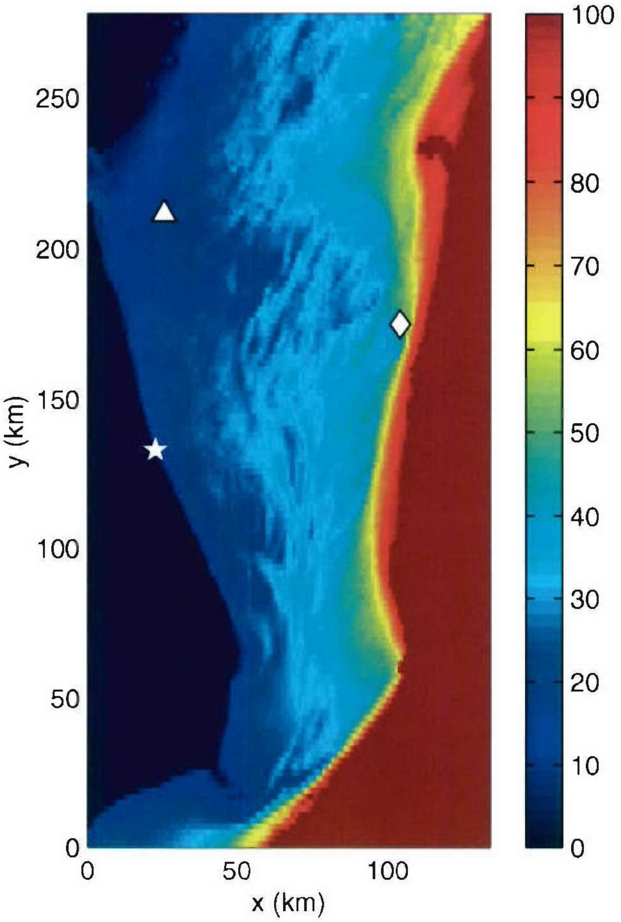

FIGURE 1. Color plot of the water depth $h(\mathbf{x})$ in meters for a region roughly centered on the USACE FRF at Duck, NC: ★, location of the FRF 8 m array; ◇, location of NDBC Buoy 44014; △, location of NDBC CHLV2 station. The x and y axes correspond to longitude and latitude, respectively, and the lower left-hand corner corresponds to 35°N 76°W

To get an indication of the results from the procedure for real-world data, it will then be used with a data set from the FRF 8m array directional spectrum as input. The resulting wave field estimate will be compared to the input data, and also to data from two NDBC buoys located in the region of interest which were not used in the assimilation procedure. The locations for these data are shown in figure 1.

To generate the synthetic data set, the SWAN model was run for the area shown in figure 1. The incident-wave spectrum was a Pierson-Moskowitz spectrum, where wind speed at 10 m above the ocean surface (U_{10}) and wind direction (θ_p)are the defining parameters. The Pierson-Moskowitz spectrum is given by

$$E(\sigma,\theta) = \alpha g^2 (2\pi)^{-4} f^{-5} \exp\left[-1.25\left(\frac{f_m}{f}\right)^4\right] \frac{1}{2}\beta \operatorname{sech}^2\left[\beta(\theta-\theta_p)\right] \tag{43}$$

where f is wave frequency, $\alpha = 0.0081$ and $f_m = 0.13g/U_{10}$ [1]. Here, the directional spread is modeled after [7] with $\beta = 2$. The example to be shown will be for a case where the wind direction, and hence the dominant wave direction, is $\theta_p = 165°$ counterclockwise from East and $U_{10} = 12$ m/s. The resulting wave spectrum is shown in figure 2a). For this spectrum, the significant wave height $H_s = 3.15$ m and the peak frequency is $f_P = 0.108$ Hz when interpolated onto the SWAN spectral grid. This spectrum was used as the input wave spectrum along the right-hand (Eastern) boundary of the region shown in figure 1. The SWAN model solution is shown in figure 2b) and 2c). Figure 2b) shows the directional spectrum at the location of the FRF 8 m array. The dominant wave direction at this location has rotated to $\theta_p = 183.3°$, roughly the cross-shore direction, and the directional spread of the spectrum has been considerably reduced relative to that shown in figure 2a). The significant wave height has been reduced to $H_s = 2.63$ m due to energy dissipation from bottom friction and depth-induced wave breaking. The resulting significant wave height field for the region is shown in figure 2c). Here, the the reduction in H_s near the upper and lower boundaries, due to the boundary conditions there, can be seen.

The spectrum from the 8 m array location was used as synthetic data, and assimilation into the SWAN model was accomplished using the methodology described above. The initial guess was assumed to be a zero incident-wave spectrum and the weighting factor on the incident wave spectrum contribution to the cost function is set at $\phi = 0.01$. The iteration history for the cost function J is shown in figure 3d) where it is seen that the cost function is reduced by roughly two decades in ten iterations of the conjugate-gradient procedure. Also shown in figure 3d) are the two separate terms in the cost function, as given by (28), where J_{obs} represents the first, 'observation', term and J_b represents the second, 'boundary', term. The contribution to the cost function from the error in the predicted spectrum at the observation location (J_{obs}) is reduced by four orders of magnitude, and is still dropping after ten iterations.

Figures 3a) and 3b) show the estimates for the incident-wave and observed directional spectra obtained from the assimilation procedure. The significant wave height for the estimated incident-wave spectrum is $H_s = 3.06$ m, about 3 percent low, and the peak frequency $f_p = 0.108$ Hz is correct, while the peak wave direction is $\theta_p = 168.8°$, which matches the true value within the directional resolution of the computations. The under-estimation of the significant wave height is at least partly due to the introduction of the incident wave spectrum E_b into the cost function; this serves to minimize the energy in the incident-wave spectrum, and hence puts downward pressure on the wave height. Figure 3b) shows the estimated directional spectrum at the FRF 8 m array location. Here, the match to the spectrum in figure 2b) is almost exact, consistent with the cost-function contribution J_{obs} in figure 3d). Also shown in figure 3c) is the estimated significant-wave-height field which shows excellent agreement with the result shown in figure 2c).

These results indicate that the assimilation procedure is capable of converging to a solution that is almost identical to those from the forward simulation which produced the data used. The results shown are for an initial guess of zero for the incident wave spectrum. An initial guess of a 'white' spectrum, constant for all wave directions and frequencies, has also been used. This produced similar results to the zero-initial-guess case, and demonstrates the uniqueness of the resulting estimated wave spectra.

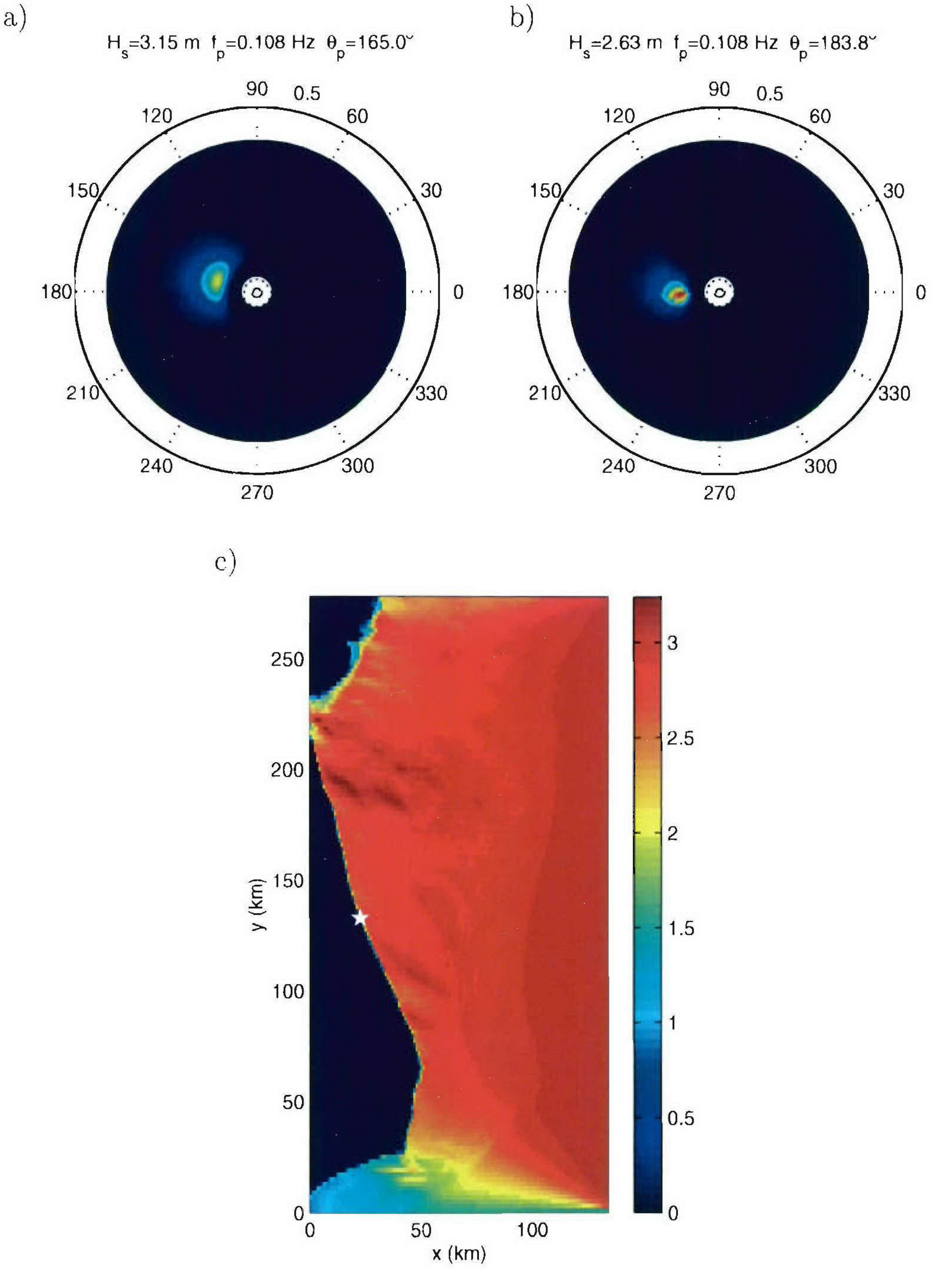

FIGURE 2. Wave directional spectra and significant wave height: a) Incident-wave spectrum applied at the right-hand (Eastern) boundary of the domain; b) SWAN-calculated spectrum at FRF 8 m array location; c) SWAN-calculated significant wave height H_s for region.

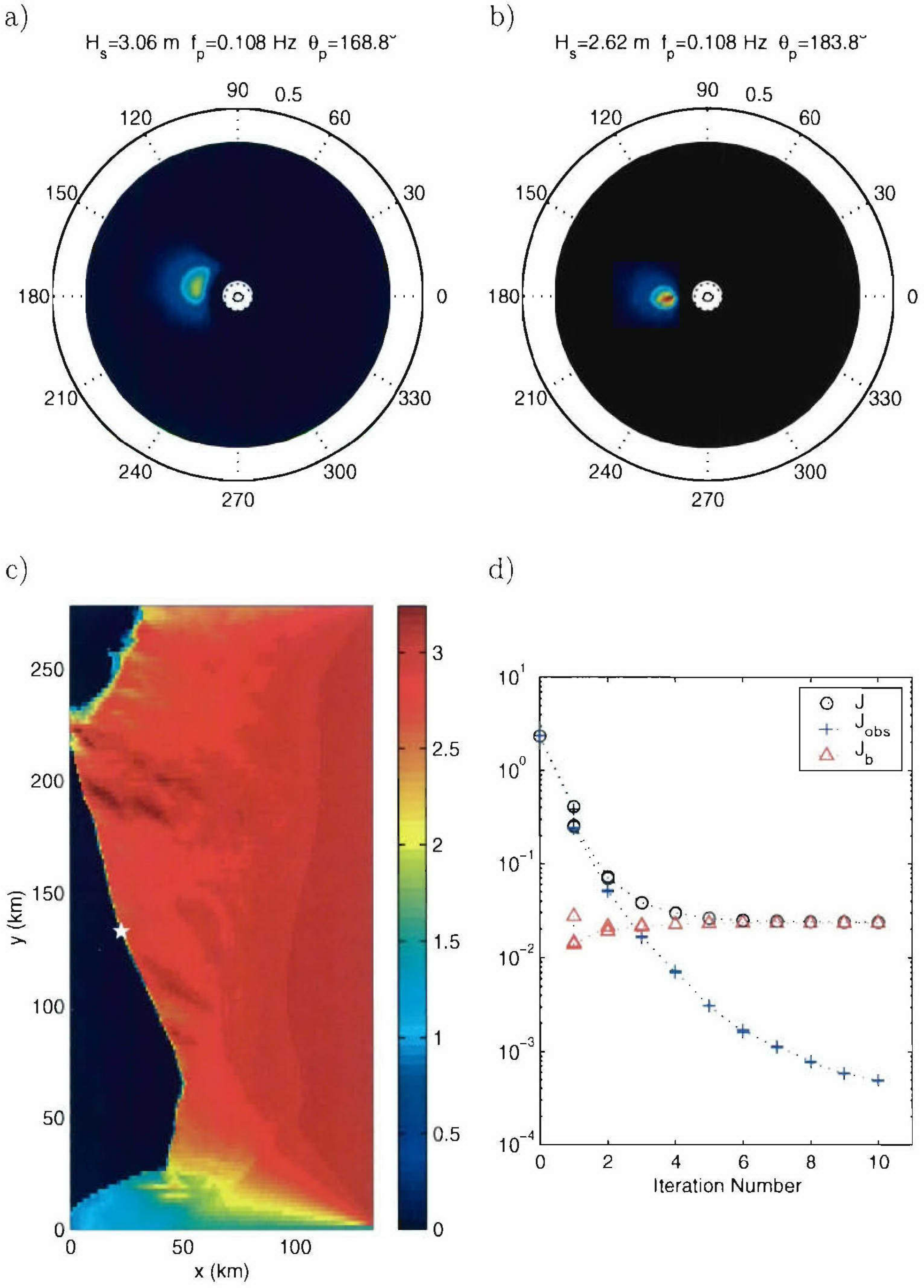

FIGURE 3. Results for assimilation of synthetic observations at the FRF 8 m array location: a) estimate of the incident-wave directional spectrum; b) estimate of the directional spectrum at the FRF 8 m location; c) resulting significant wave height for region; d) iteration history for the cost function J, along with its two components defined in (28).

Application to Wave-Spectrum Observations

The foregoing example showed that the assimilation procedure works well for synthetic data. To demonstrate its potential for real-world applications, it will now be applied to a measured directional-spectrum data set from the FRF 8 m array. The resulting estimates of the wave spectra and their integral properties will be compared to both those of the 8 m array spectrum, and those from two NDBC measurement stations located in the region: NDBC 44014 which is located to the Northeast of the observation location offshore near the continental shelf break, and CHLV2 near the entrance to the Chesapeake Bay, in shallower water. These NDBC instruments provide frequency spectra, and estimates of the integral parameters of the spectra.

Figure 4 shows the results for assimilation of a directional spectrum for 13 September 2001 at 01:00 EST. Here again $\phi = 0.01$ and ten conjugate-gradient iterations are used. For this case the significant wave height was $H_s = 1.58$ m, the peak frequency was $f_p = 0.089$ Hz and the mean frequency was $f_m = 0.130$ Hz. The peak wave direction was $\theta_p = 183.8°$, the mean direction at the peak frequency was $\theta_{m,p} = 187.3°$ and the mean wave direction was $\theta_m = 188.6°$. The directional spectrum is shown in figure 4a). The estimated directional spectrum from the assimilation procedure which corresponds to this observation is shown in figure 4b) where the significant wave height is lower by about six percent ($H_s = 1.48$ m) and the wave direction by all three measures used above is estimated within two degrees. The peak frequency matches the observations, but the mean frequency is slightly lower, indicating that the lower wave height is due to lower energy at high frequencies; a conclusion supported by comparison of figures 4a) and b). Figure 4c) shows the estimated significant wave height field for the region. In this case, the waves are propagating nearly East to West and, as a result, there are triangular regions at the North and South boundary where the wave-height predictions are erroneously low. The iteration history of for the cost function J is shown in figure 4d). In this case the cost function decrease is slightly more than an order of magnitude; this is mainly due to the reduction in the relatively high contribution from the observation J_{obs}, which plateaus after about seven iterations. This is indicative of the shortcomings in the SWAN model physics when compared to real-world data; however, the overall agreement as shown above is quite good.

A more stringent test of the assimilation procedure is whether the estimated wave field matches observational data other than that used as input. For this, contemporaneous NDBC wave data is used. Figures 5a) and b) show the direction spectra for the two NDBC locations, 44014 and CHLV2, respectively.

Figure 5c) shows a comparison of the wave frequency spectra from NDBC 44014 and SWAN, where the SWAN spectra are calculated by integrating the frequency-direction spectra in θ. The general shape of the spectrum is quite well captured although for frequencies near the peak and lower, SWAN slightly under-estimates the spectrum. The peak frequency is $f_p = 0.090$ Hz from the data while SWAN predicts $f_p = 0.081$ Hz, which agrees to within the resolution of the two discretizations of the spectrum. Comparing integral parameters, it is seen that SWAN under-estimates H_s by some twenty percent ($H_s = 1.59$ m vs. 2.00 m); this is due to the under-estimation of the spectrum at low frequencies and, to a lesser extent, to the fact that the 44014 spectrum extends to higher frequency than the SWAN spectrum grid. The mean frequencies agree to within three percent ($f_m = 1.37$ Hz for 44014, and

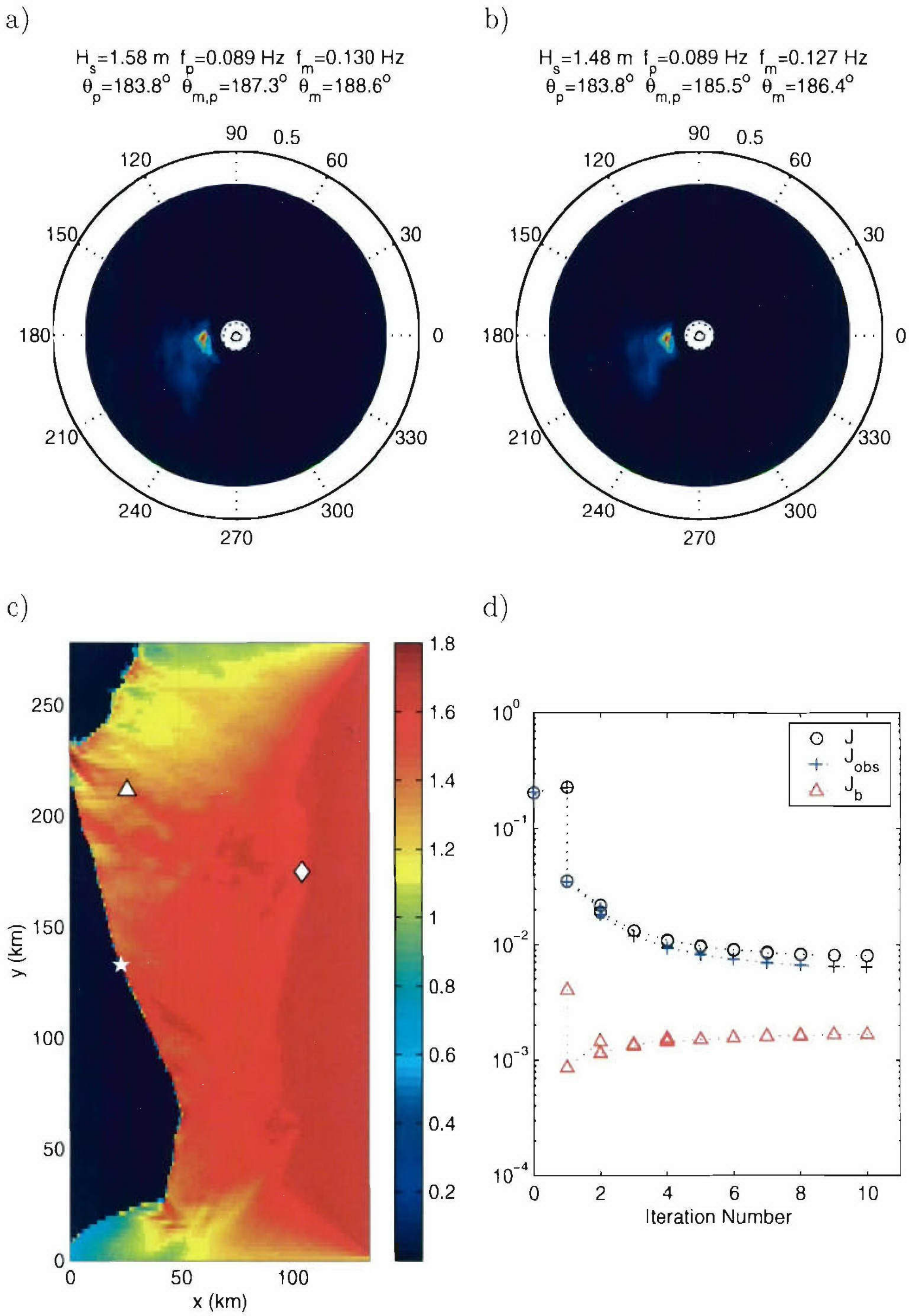

FIGURE 4. Results for assimilation of a measured wave spectrum at the FRF 8 m array location for 13 September 2001 at 01:00 EST: a) measured FRF directional spectrum; b) estimate of the FRF directional spectrum; c) resulting estimate of the significant wave height H_s for region; d) iteration history for the cost function J, along with its two components defined in (28).

1.34 Hz for SWAN). The mean wave direction at the peak frequency is $\theta_{m,p} = 185.0^\circ$ for 44014 and 184.5° for SWAN. Overall the agreement is excellent and, since NDBC 44014 is located off-shore near the shelf-break, this indicates that the assimilation procedure does a good job in estimating the incident-wave spectrum

Figure 5d) shows a similar comparison of the wave frequency spectra from NDBC CHLV2 and SWAN. Here, the shape of the spectrum is reasonably well-captured; however, the peak is over-estimated by a factor of three. This is balanced by under-estimates of the energy density at higher frequency (and the extreme low-frequency tail) to produce a significant-wave-height estimate of $H_s = 1.41$ m from SWAN, compared to 1.40 m for CHLV2. The peak frequency is $f_p = 0.100$ Hz from CHLV2, compared to the SWAN estimate of 0.081 Hz. The mean frequency f_m is again lower for SWAN (0.120 Hz), than for CHLV2 (0.169 Hz); this is due to the observed under-estimation of the spectrum at high frequencies. Comparison of wave direction estimates are not possible, since CHLV2 only provides frequency information.

From the foregoing, it is clear that the comparisons of the assimilation results to data from NDBC buoy 44014 and station CHLV2 produce mixed results. The agreement is very good for 44014, while for CHLV2, it is somewhat less satisfying. Examination of the locations of 44014 and CHLV2 relative to the FRF 8 m array and CHLV2 (see e.g. figure 5c) and the fact that the wave direction indicated by the off-shore buoy 44014 is $\theta_{m,p} = 185^\circ$, would seem to indicate that if the spectrum is accurately estimated at the location of 44014, it would be reasonably accurate at both the FRF location and CHLV2. Good agreement with the data is found at the FRF location, but not CHLV2. The reason for this is apparent in figure 5c), which shows a drop in significant wave height in the vicinity of CHLV2, and to the North. CHLV2 appear to be located in the region near the upper boundary where the wave-height will be under-estimated due to boundary effects. Be that as it may, the key to obtaining an accurate regional estimate of the wave field, is accurately determining the off-shore, incident-wave spectrum. The excellent results obtained in the comparison to NDBC 44014, indicates the promise of this approach.

4.2 Estimation of the Wave Field from SAR Observations

We now apply the assimilation procedure to estimate wave spectra from SAR-image data, in particular, to SAR-image-spectrum data. We will focus on SAR-image data for the region around the USACE Field Research Facility in Duck NC. Figure 6 shows an ERS SAR image overlaid on the bathymetry contours for the region containing the FRF site. The image is roughly 100 km on a side and it reaches from the land out to the edge of continental shelf. The image is oriented to reflect the SAR look direction (the cross-track direction) of -78.1°T and, due to the orbit geometry, the satellite passes over this region at 10:44 EST.

Waves are often apparent in SAR images, as seen in Figure 7, which shows a close-up of the near-shore region in the SAR image shown in 6. Waves propagating cross-shore, with crests oriented parallel to the shore, are clearly visible. Also apparent is speckle noise due to the coherent nature of the SAR imaging process. Speckle is a major source of noise in the SAR assimilation process. Figure 8 shows the directional ($\mathbf{k}$) spectrum of a 1.6 km-square subset of the the SAR image. The wave propagation direction is clearly indicated by the spectral peak; however, since the SAR image is essentially a snapshot, there is a 180° propagation-direction ambiguity. Also evident is point-to-point variability expected in

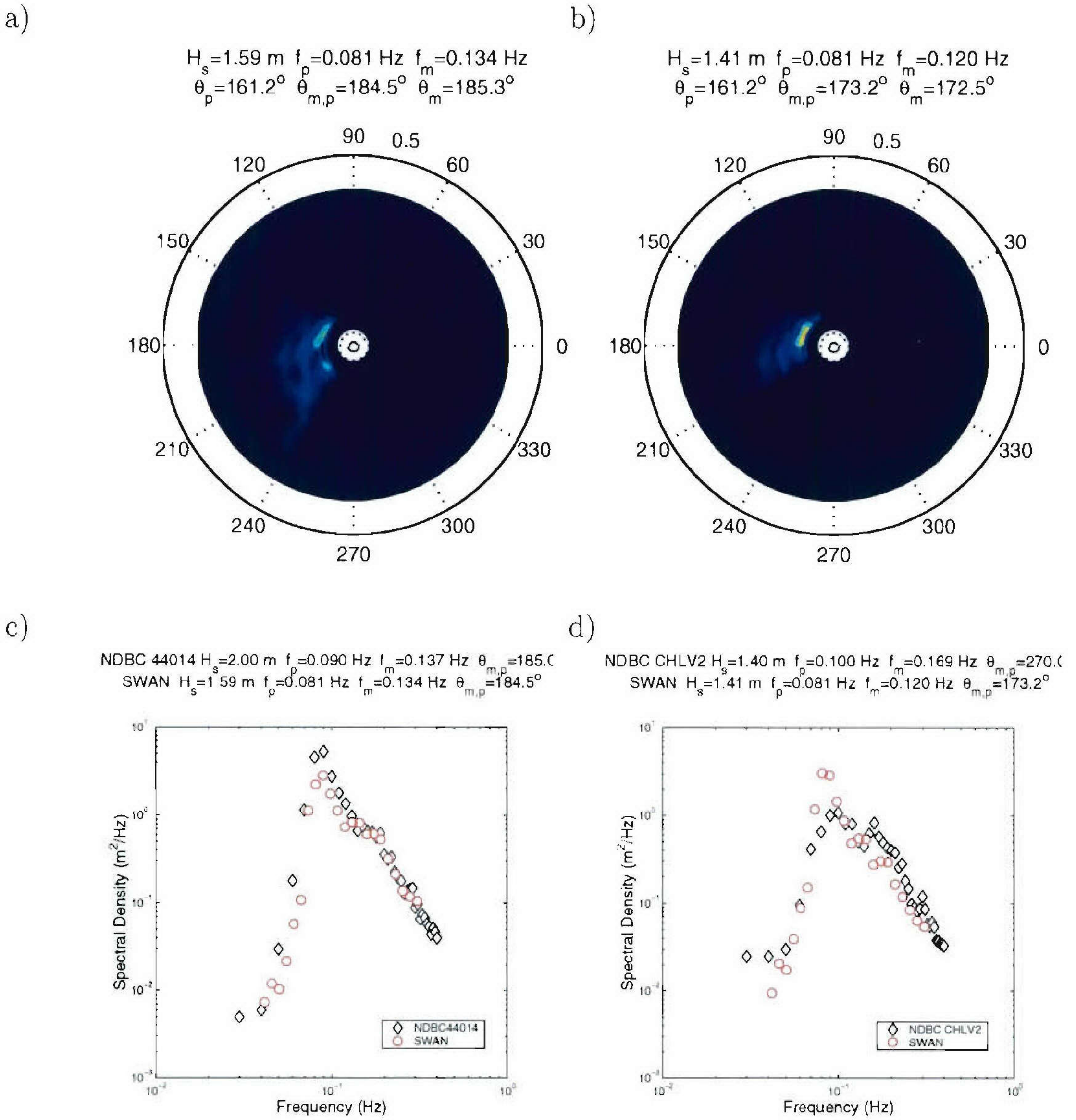

FIGURE 5. Results for assimilation of a measured wave spectrum at the FRF 8 m array location for 13 September 2001 at 01:00 EST and comparison of to NDBC buoy data: a) estimate of directional spectrum for location of NDBC 44014; b) estimate of directional spectrum for location of NDBC CHLV2; c) comparison of estimated one-dimension directional spectrum to data from NDBC 44014; d) comparison of estimated one-dimension directional spectrum to data from NDBC CHLV2.

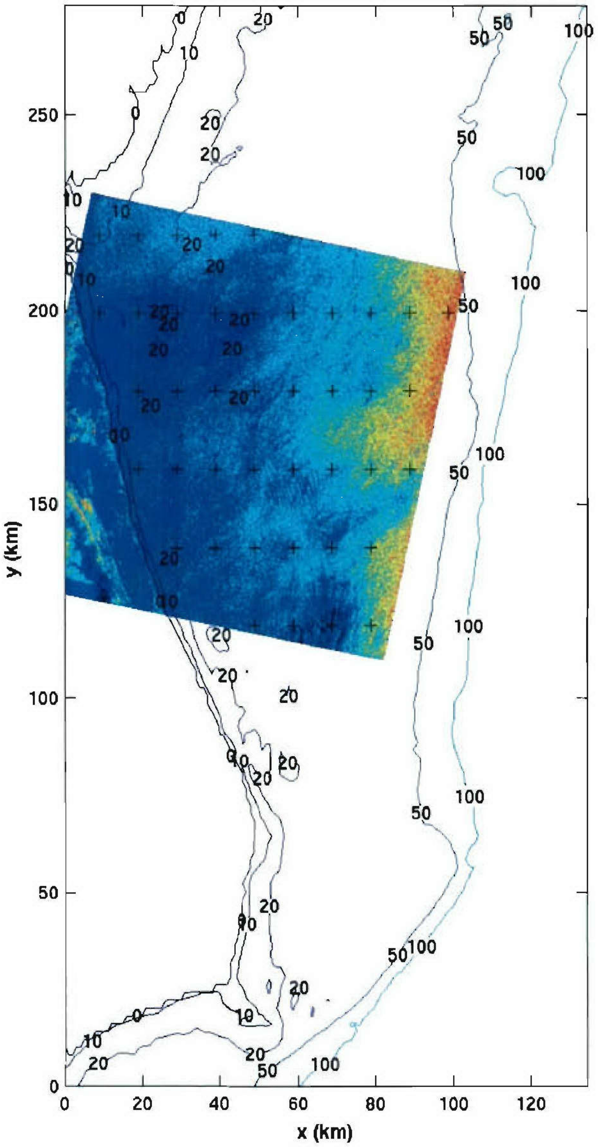

©1997 ESA

FIGURE 6. Example of an ERS SAR image overlaid on the bathymetry contours for the region around the USACE FRF; + indicates the locations of the SAR spectrum observations used for assimilation. The SAR look direction is $-78.1°$T (the $+y$ axis points North) and the satellite track is oriented at 191.9°T.

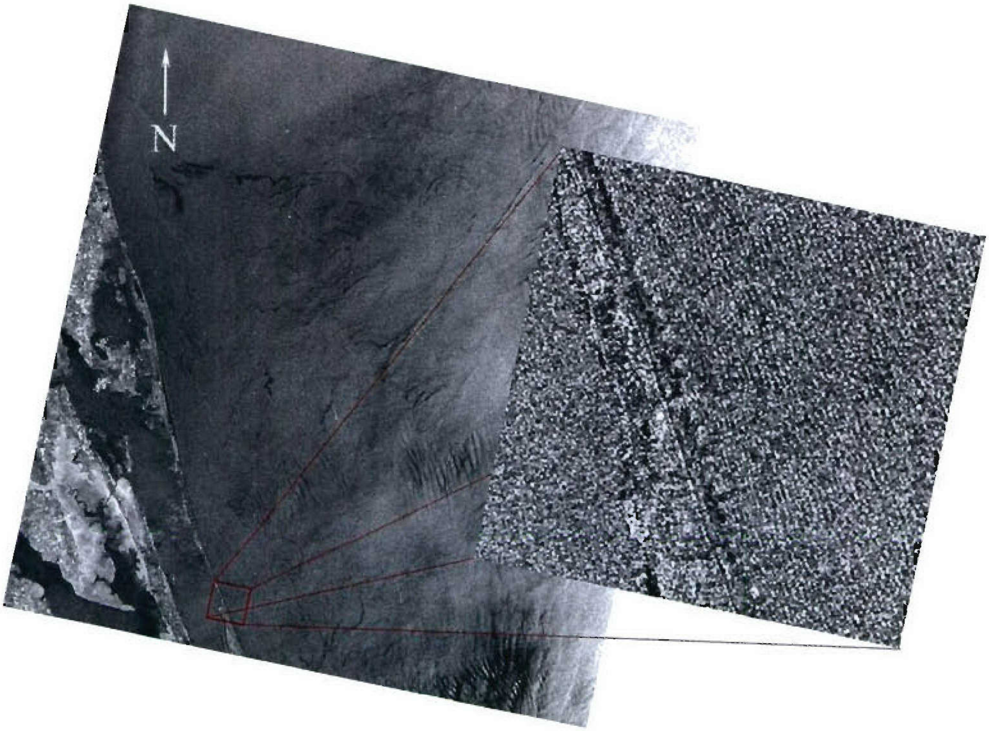

©1997 ESA

FIGURE 7. Magnified view of near-shore waves for the SAR image shown above in figure 6.

a spectral estimate based on a finite-size region.

Application to Simulated SAR-Spectrum Data

To evaluate the assimilation procedure, independent of complications due to errors in both the wave-field and the SAR image modeling, it is first applied to a set of simulated observations. The wave spectrum calculated using the SWAN model for 41 locations in (indicated by the crosses in figure 6, above) was used along in the nonlinear SAR model to generate the observations. The results are shown in figure 9. The cost function history indicates that the cost function decreases by about two orders of magnitude in about twenty-five iterations, and so there is a good match between the predicted SAR spectrum and the simulated observations. Since there is no noise in added to the data, the errors are indicative of information lost in going from the wave spectrum to the SAR-image spectrum, as a result of imaging effects. Also shown in figure 9 is a comparison between the estimated and actual wave spectra at the location of the FRF 8 m array. The peak frequency is well-estimated and the peak wave direction is within about 7°. The significant wave height is under-estimated by nearly 20 percent, mainly due to high-frequency waves which are lost in the SAR-imaging process. It should be noted that this is best-case performance, but it indicates that the assimilation procedure is convergent and capable of estimating the wave spectrum from SAR-image spectrum observations.

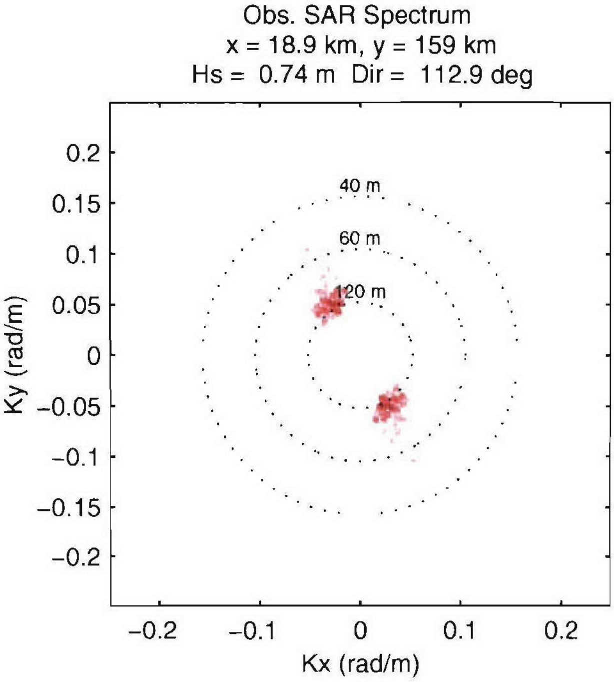

FIGURE 8. Sample SAR-image spectrum from the near-shore region. Here the spectrum has been rotated and the SAR look direction is aligned with the k_y axis.

Application to SAR-Spectrum Observations

We now apply the assimilation procedure to SAR-image spectrum data from ERS imagery. For each of the results shown below, 41 1.6 km square (128x128 pixel) subsets were extracted from the SAR image at selected SWAN grid points. These subsets were Fourier transformed and the and the image power spectra were calculated. Starting from an assumed zero, the incident wave spectrum was estimated via the assimilation procedure. The final estimate of incident spectrum is that which produces the best-fit of the estimated SAR spectra (using equation 11) to the observed spectra, calculated from the imagery. For these purposes, the best fit was achieved when the cost function ceased to decrease, and levelled off. In the results below, the resulting wave field estimate is evaluated by comparing to contemporaneous data from the FRF 8 m-array.

The first image is from 05 March 1997 at 10:44 EST; this is the SAR imagery shown above in figures 6 and 7. Results for the assimilation procedure are shown in figure 10. The cost function is reduced by more than half, not quite as good as the results obtained with simulated data. The estimated significant-wave-height field is also shown, where a wedge of low wave height is seen near the Northern boundary; this is due to the Southwesterly wave propagation direction. The estimated wave spectrum for the location of the FRF 8 m array is also shown in figure 10, along with the contemporaneous in-situ spectrum. The estimated peak wave direction and the peak frequency compare favorably with the in-situ data, with the peak frequency within five percent and the peak direction within 8°; however, the significant wave height is under-estimated by more than 30 percent. This is due to the

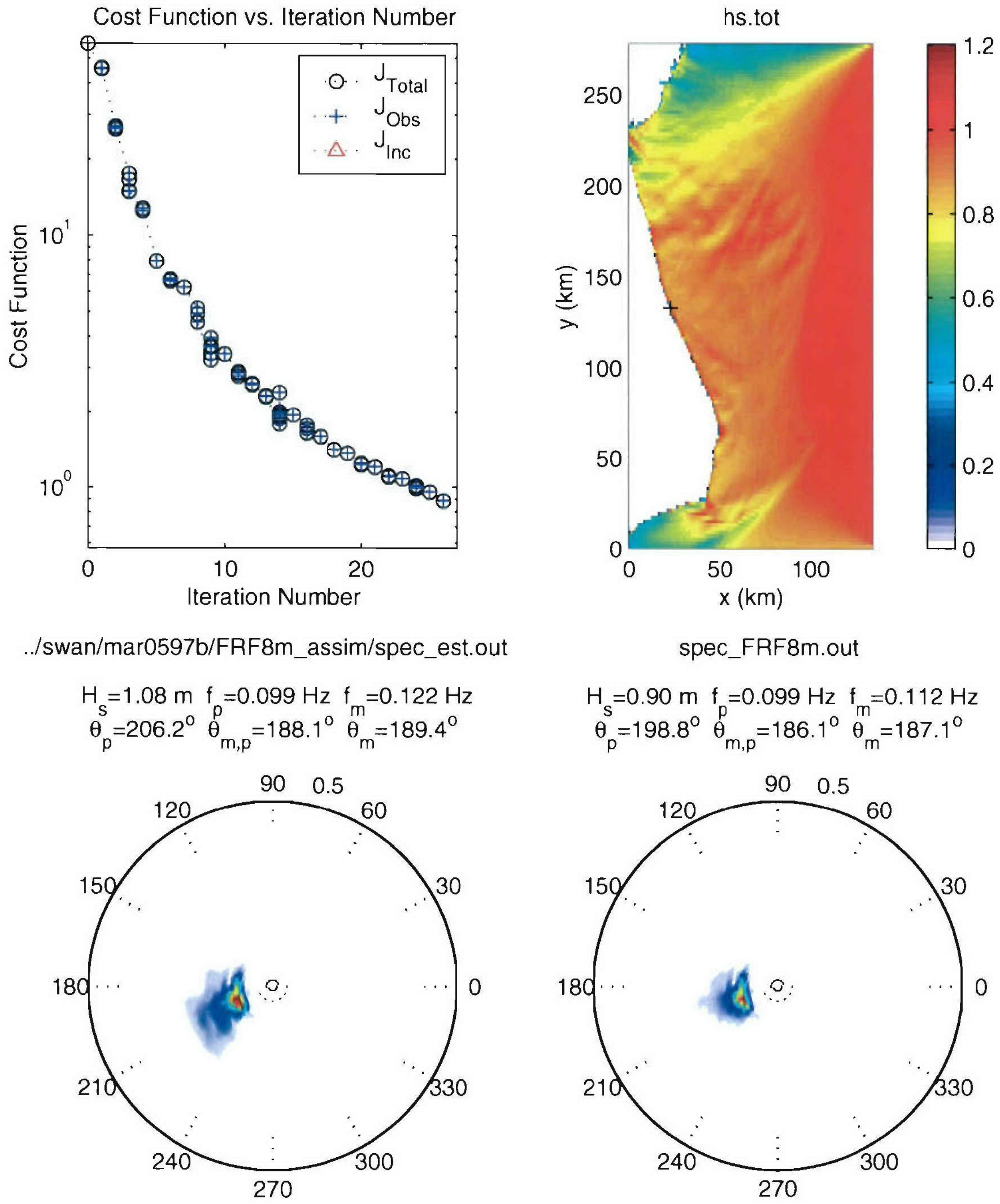
Cost Function vs. Iteration Number

hs.tot

../swan/mar0597b/FRF8m_assim/spec_est.out

H_s=1.08 m f_p=0.099 Hz f_m=0.122 Hz
θ_p=206.2° $\theta_{m,p}$=188.1° θ_m=189.4°

spec_FRF8m.out

H_s=0.90 m f_p=0.099 Hz f_m=0.112 Hz
θ_p=198.8° $\theta_{m,p}$=186.1° θ_m=187.1°

FIGURE 9. Results for assimilation of simulated SAR data for the region around the USACE FRF; upper left: cost function iteration history; upper right: estimated significant wave height; lower right: estimated spectrum; lower left, actual simulated spectrum. Locations of SAR spectrum observations used for assimilation are shown in 6.

smaller directional spread and frequency width of the estimated spectrum. This is due to the loss of high-frequency (short wavelength) waves wave information in the SAR imagery, as well as information at high azimuth (along-track) wavenumbers.

A sample of the spectrum results from the assimilation procedures are shown in figure 11. These results are for a location near the shore. The figure shows the estimated wave spectrum, the SAR spectrum estimate calculated from that wave spectrum, the actual SAR spectrum observation, and difference between the estimated and observed SAR spectrum. This latter quantity provides the input into the adjoint model. From the figure it is clear that the estimated SAR spectrum compares well with the observed spectrum, the main difference results from the speckle noise present in the observed spectrum.

Results for assimilation of an ERS SAR image from 09 April 1997 are shown in figure 12. For these data, the cost function drops only a few percent over eight iterations and the the estimated significant wave height is only 0.4 m or less. Comparison of the estimated and actual wave spectra for the FRF 8 m array shows that the actual wave height at this location is 1.38 m vs. the estimate of 0.3 m. The reason for this discrepancy can be found in the observed FRF spectrum — the dominant wave direction is 209.9°T, 73° from the SAR look direction, and the waves are relatively high frequency ($T_p \leq 6$ sec). Hence, the wave energy is mainly outside the azimuth pass-band of the SAR-imaging process. It is interesting to note that the small amount of energy near the SAR pass-band is captured by the assimilation procedure. This is an example where the information lost in the SAR imaging process cannot be retrieved by the assimilation procedure.

Figure 13 shows the results for another SAR image from 03 July 1996. For this case, the waves are out of the Southeast with a significant wave height of less than a meter. The assimilation procedure converges, when the cost function is reduced by about one-third. For the FRF 8 m-array location, the estimated wave height is 0.54 m, compared to the actual wave height of 0.68 m, the estimated peak frequency $f_p = 0.108$ Hz is within five percent of the actual, and the estimated peak wave direction $\theta_p = 272°\text{T}$ differs by about 12° from the actual. Comparing the directional spectrum plots shows that the under-estimation of the significant wave height is again due to the loss of wave energy at higher frequencies and larger angles relative to the SAR look direction. The discrepancy in the estimated peak wave direction seems less pronounced if the width of the spectral peak is taken into account — the data show a broad, slightly bi-modal peak, where the estimate shows a corresponding broad, but uni-modal, peak in in the same location.

The final result is from 14 May 1997 and has waves again propagating from the Southeast with a comparable significant wave height, about half a meter. The results for assimilation of this image are shown in figure 14. The cost function in this case is reduced by about 40 percent at convergence and the agreement is excellent for wave height, frequency and direction.

4.3 Estimation of Bottom Friction from SAR Observations

The above results for estimation of the wave field from SAR observations indicates that there is sufficient information contained in the SAR imagery to get a reliable estimate of the waves. We wish to extend this estimation capability to the the bottom friction coefficient $C_b(\mathbf{x})$. We do this using a similar approach to the above, but now we include adjustments in the

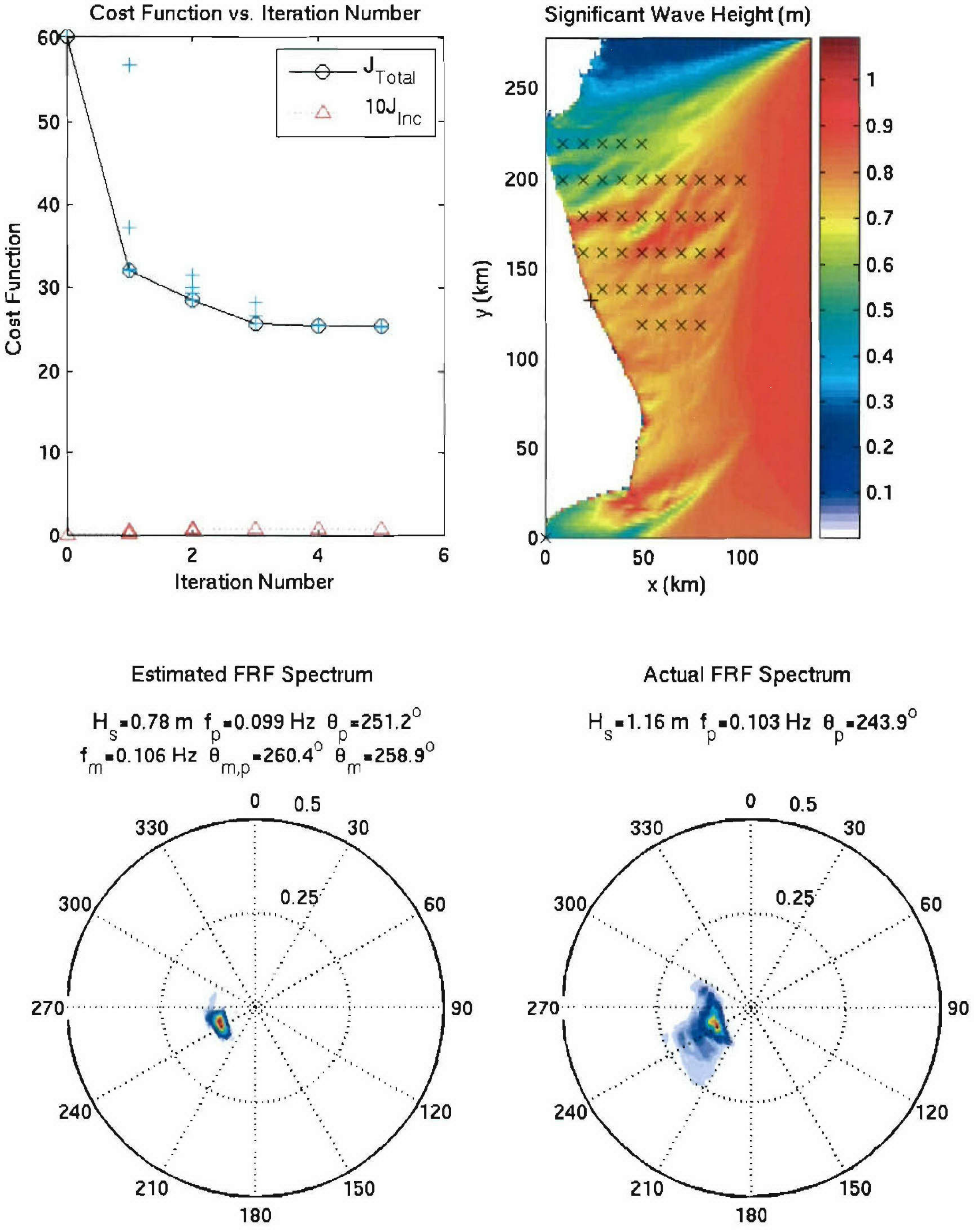

FIGURE 10. Results for ERS SAR data for 05 March 1997 10:44 EST for the region around the USACE FRF; × indicates the locations of the SAR spectrum observations used for assimilation and +indicates the location of the FRF 8 m array.

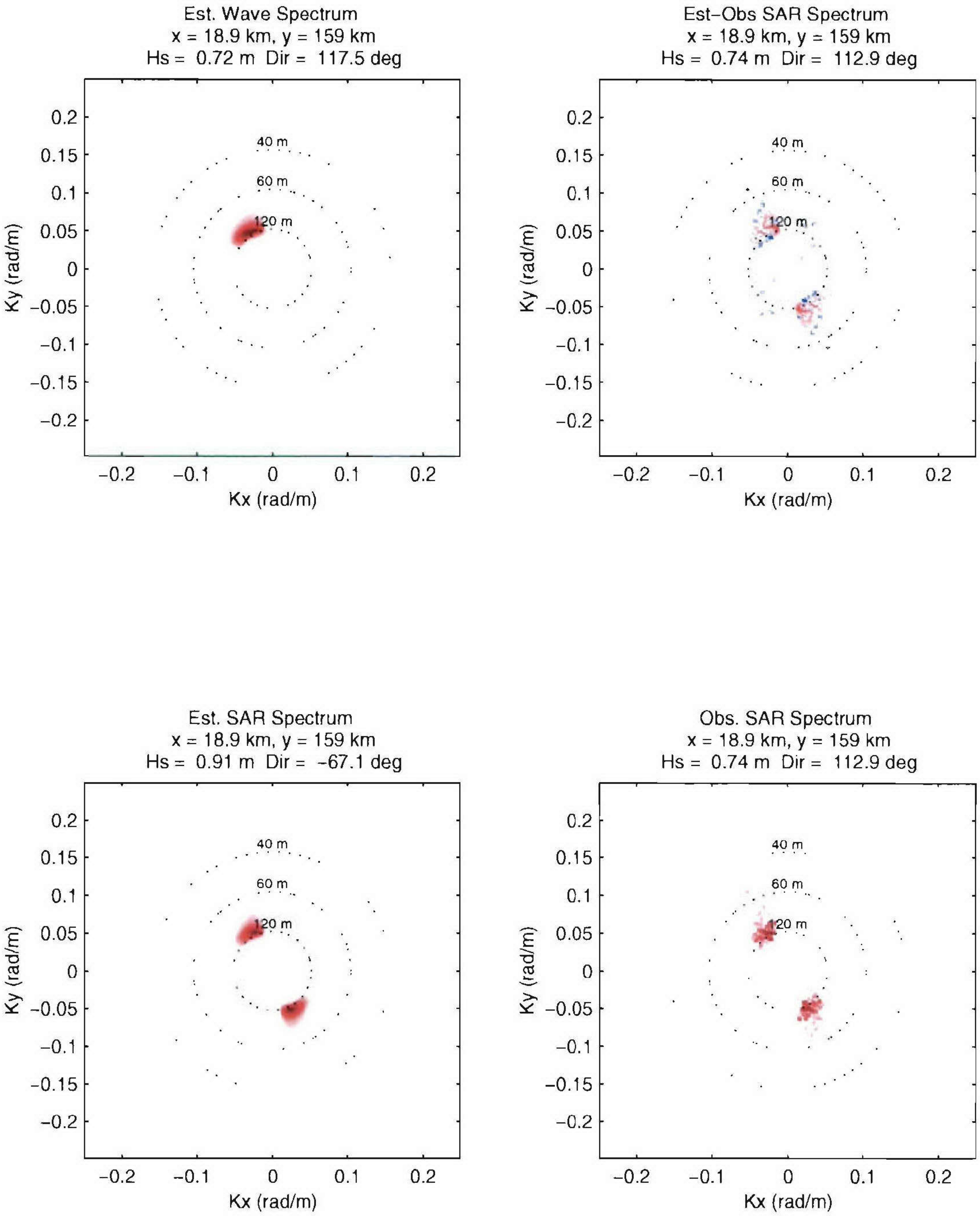

Est. Wave Spectrum
x = 18.9 km, y = 159 km
Hs = 0.72 m Dir = 117.5 deg

Est-Obs SAR Spectrum
x = 18.9 km, y = 159 km
Hs = 0.74 m Dir = 112.9 deg

Est. SAR Spectrum
x = 18.9 km, y = 159 km
Hs = 0.91 m Dir = -67.1 deg

Obs. SAR Spectrum
x = 18.9 km, y = 159 km
Hs = 0.74 m Dir = 112.9 deg

FIGURE 11. Sample detailed results from the assimilation procedure for $x = 18.9$ km and $y = 159$ km: the estimated wave spectrum, the estimated SAR-image spectrum, the observed SAR-image spectrum, and the difference between the estimated and the observed SAR-image spectra. Here, red is positive, blue is negative, zero is white, and the SAR look direction is aligned with the k_y axis.

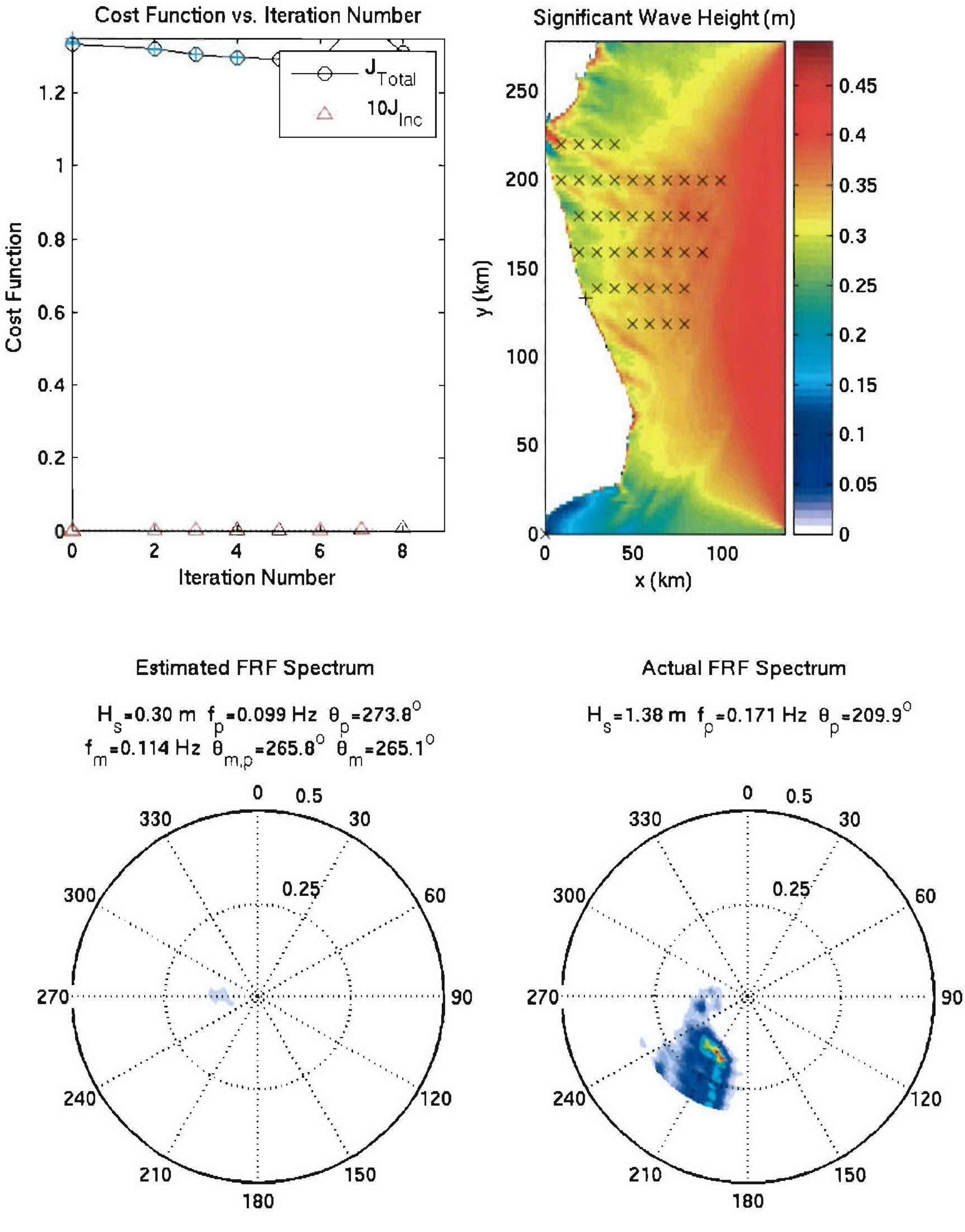

FIGURE 12. Results for ERS SAR data for 09 April 1997 10:44 EST for the region around the USACE FRF; × indicates the locations of the SAR spectrum observations used for assimilation and +indicates the location of the FRF 8 m array. For this case, the wave energy falls substantially outside the SAR pass-band.

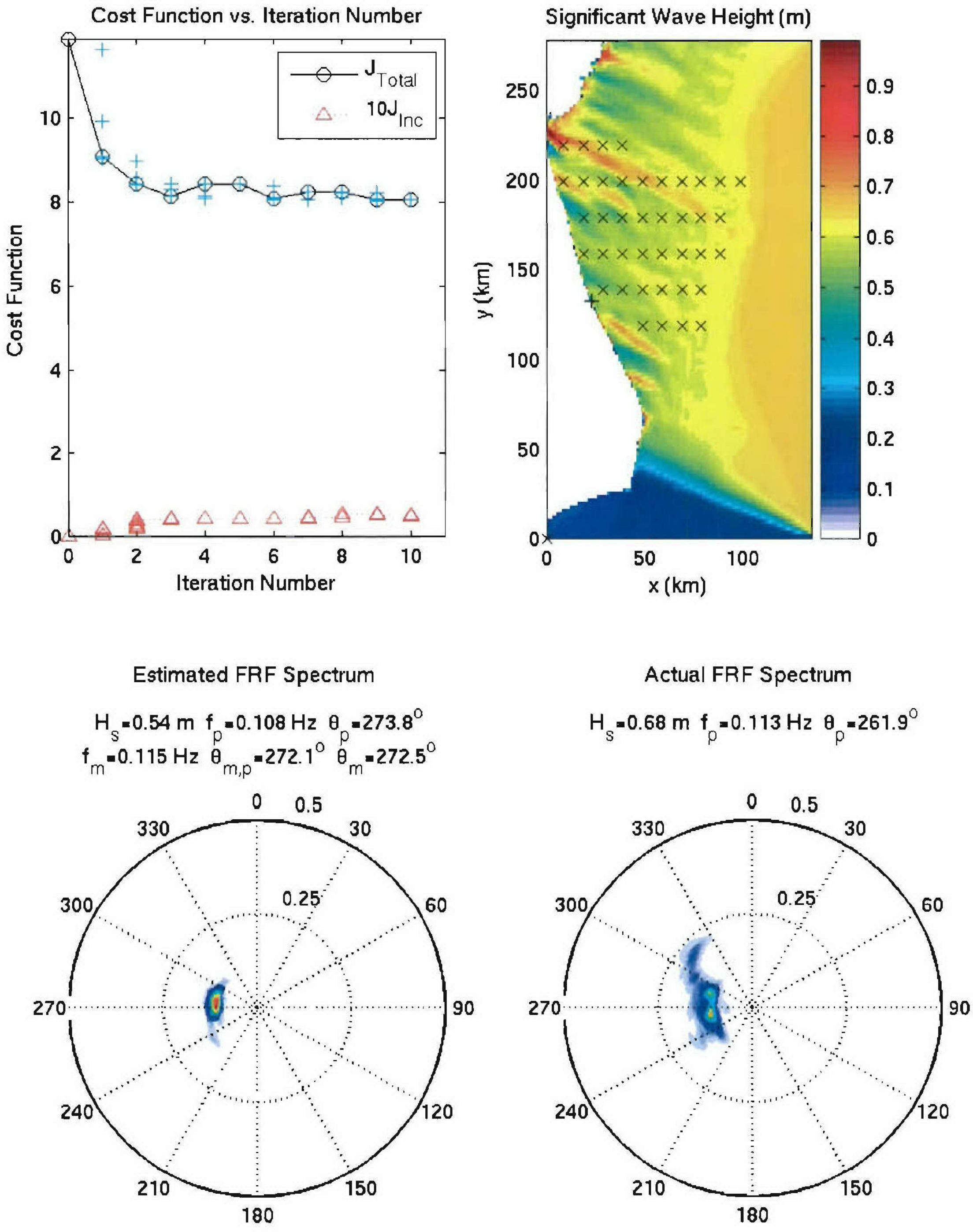

FIGURE 13. Results for ERS SAR data for 03 July 1996 10:44 EST for the region around the USACE FRF; × indicates the locations of the SAR spectrum observations used for assimilation and +indicates the location of the FRF 8 m array.

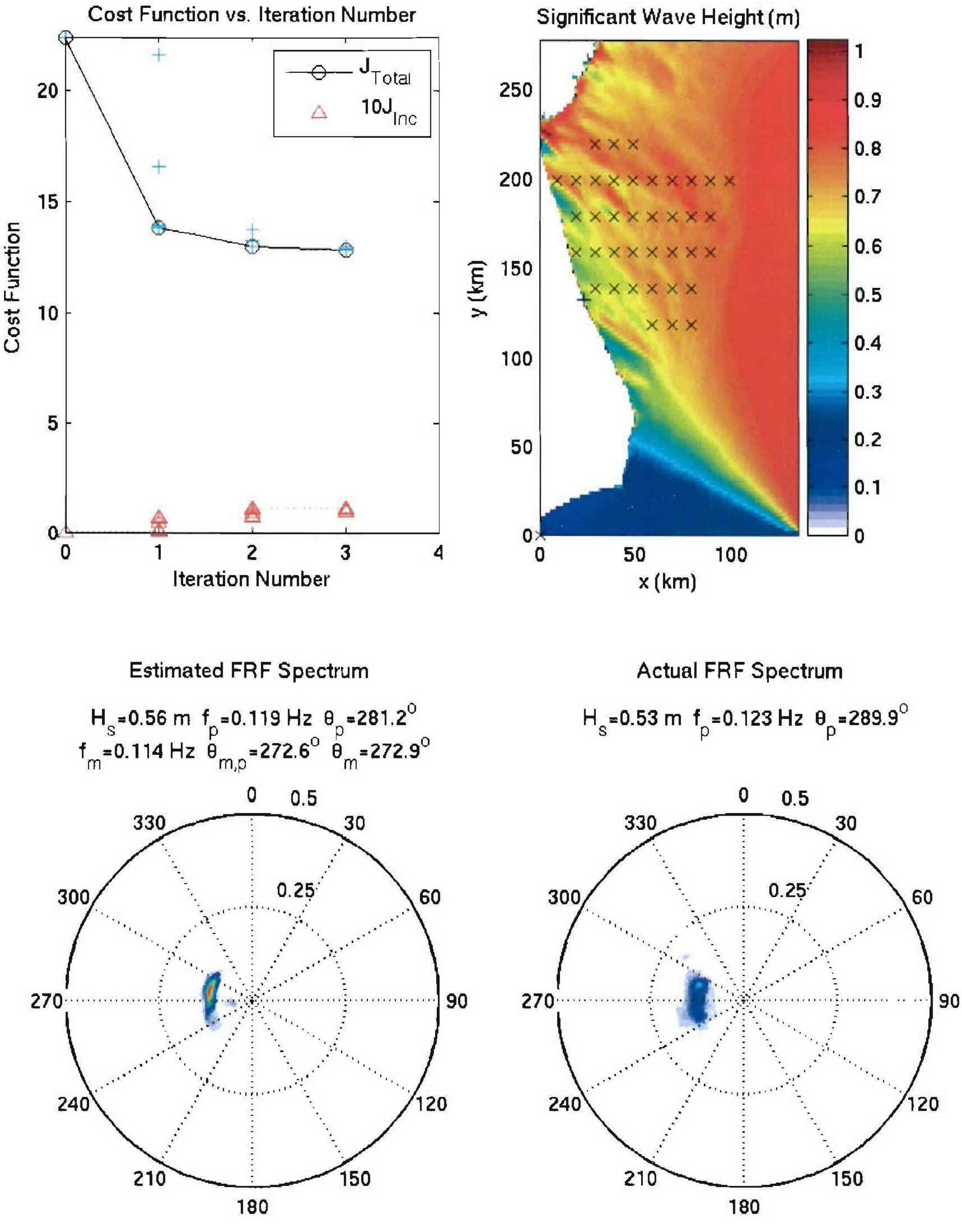

FIGURE 14. Results for ERS SAR data for 14 May 1997 10:44 EST for the region around the USACE FRF; × indicates the locations of the SAR spectrum observations used for assimilation and +indicates the location of the FRF 8 m array.

bottom friction coefficient calculated using (42) at each iteration. This was applied the SAR imagery from 14 May 1997 assuming an initial friction coefficient of $C_b = 0.0015$, the default for the SWAN model. Figure 15 shows results, the r.m.s. bottom velocity (used in the friction model) and the friction coefficient $C_b(\mathbf{x})$ estimated using the assimilation procedure. The assimilation procedure indicates that the the friction coefficient should increase by about 30% as the shore is approached in the region of the SAR image observations. Additional results are shown in figure 16, where it is seen the cost-function reduction is similar to that achieved above when bottom friction was not considered, but the off-shore significant wave height is much larger than before. Even though the off-shore significant wave height is larger than previously estimated, the agreement between the estimated and actual FRF spectra is similar to that obtained without consideration of the bottom friction.

These results indicate that the estimation of the bottom friction coefficient from SAR imagery using variational assimilation is feasible, but it must be applied more broadly to determine the robustness and accuracy of the procedure.

5 Summary and Conclusions

A variational assimilation procedure for near-shore waves using the SWAN model has been described. The assimilation procedure can be applied to wave spectrum observations or SAR-image spectra obtained from satellite-based sensors. For SAR assimilation, the SWAN model is augmented with the Hasselmann & Hasselmann [10] nonlinear model relating the SAR-image spectrum to the local wave spectrum. The assimilation procedure is used to estimate the incident-wave spectrum at the boundary, and alternatively the bottom friction coefficient, which produces the best fit between the model predictions and the data.

Results for wave-spectrum observations are shown for synthetic observational data, as well as actual data. Application to synthetic data shows that the assimilation methodology can be used to accurately determine a spatially uniform incident-wave spectrum based on a single near-shore spectrum observation. For real-world spectrum data from the FRF 8 m array, the results yield a good fit to the observational data, and compare reasonably well to NDBC Buoy observations.

Results for SAR-image-spectrum observations are also shown for synthetic observational data and actual data. Application to synthetic data shows that the assimilation methodology can be used to accurately estimate the wave spectrum from an array of simulated SAR-image spectra; the main error is the loss of some high-frequency wave energy. When applied to an array of SAR-image spectra obtained from ERS satellite-based SAR imagery, the results are similarly good, but when the waves are propagating at large angles relative to the SAR look direction, the wave energy does not appear in the SAR-image spectrum due to well-known SAR-imaging effects, and cannot be retrieved.

The use of SAR assimilation for the estimation of the bottom friction coefficient and resulting energy dissipation was investigated and the results appear to be promising, but more extensive application is required to determine the robustness and overall validity of the estimation procedure.

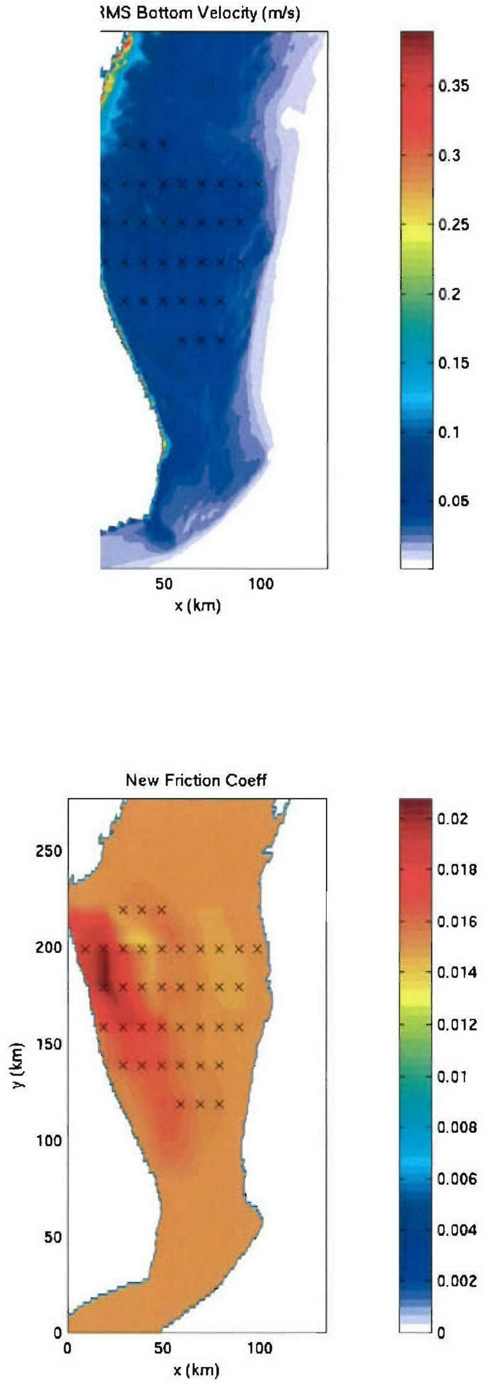

FIGURE 15. Results for estimation of bottom friction from ERS SAR data for 14 May 1997 10:44 EST: r.m.s. bottom orbital velocity used in the friction model and estimated bottom friction coefficient C_b showing an increased level in the near-shore region.

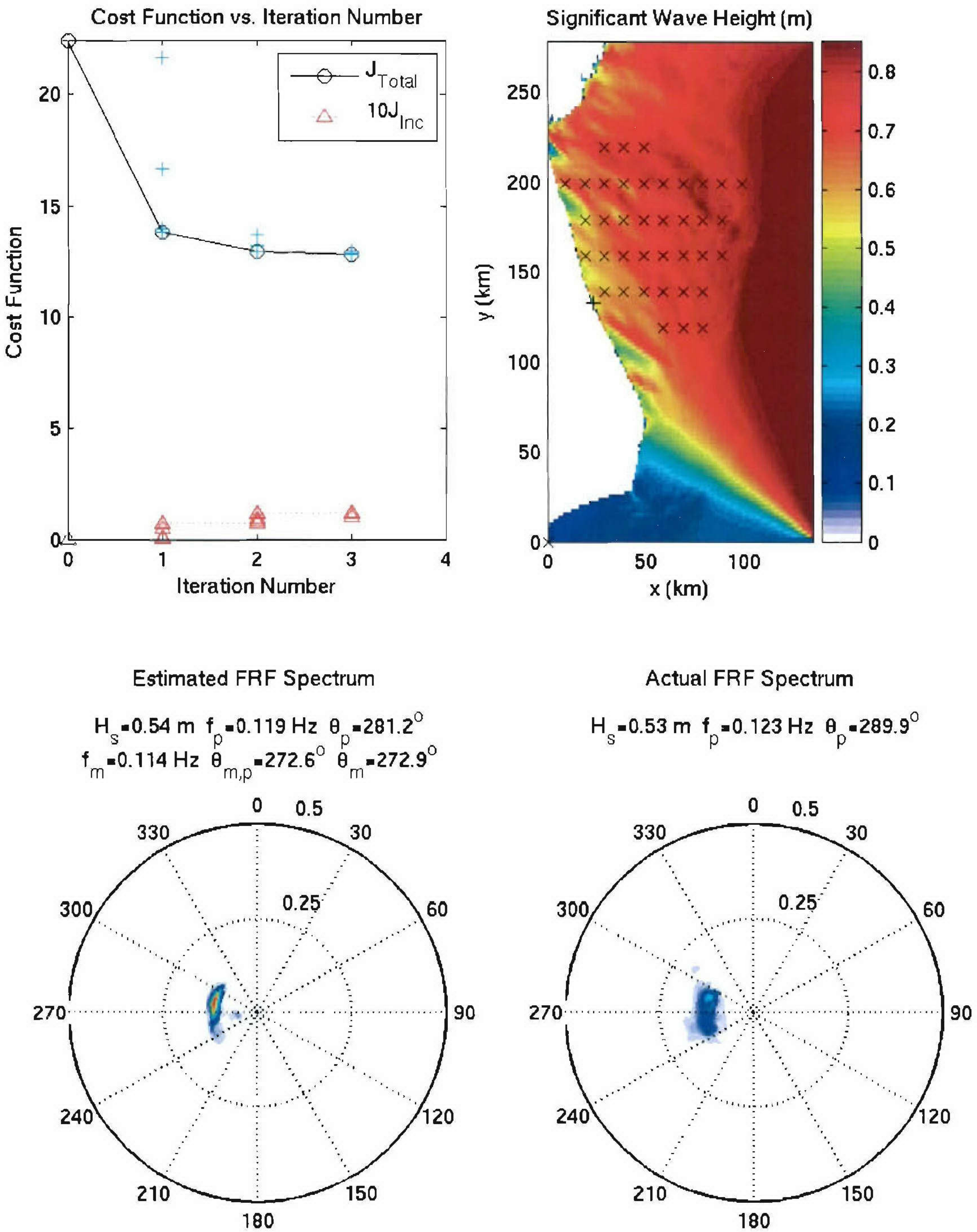

FIGURE 16. Results for the cost function and wave field for assimilation of ERS SAR data for 14 May 1997 10:44 EST with bottom-friction estimation; × indicates the locations of the SAR spectrum observations used for assimilation and +indicates the location of the FRF 8 m array.

References

[1] Alves, J.H.G.M and M.L. Banner, Revisiting the Pierson-Moskowitz asymptotic limits for fully developed wind waves, *J. Phys. Oceanography.*, *33*, 1302, 2003.

[2] Bennett, A.F., *Inverse Methods in Physical Oceanography,* Cambridge, 1992.

[3] Bennett, A.F., and R.N. Miller, Weighting initial conditions in variational assimilation schemes, *Monthly Weather Rev., 119*, 1098, 1991.

[4] Booij, N., R.C. Ris and L.H. Holthuijsen, A third-generation wave model for coastal regions: 1. Model description and validation, *J. Geophys. Res., 104*, 7649, 1999.

[5] Collins, J.I., Prediction of shallow water spectra. *J. Geophys.Res.* 77, 2693-2707, 1972.

[6] Courant, R. and D. Hilbert, *Methods of Mathematical Physics,* Wiley Interscience, 1953.

[7] Donelan, M.A., Hamilton, J. and Hui, W.H., Directional spectra of wind-generated waves, *Phil. Trans. R. Soc. Lond., A 315*, 509, 1985.

[8] Hasselmann, K., Measurements of wind-wave growth and swell decay during JONSWAP, *Dtsch. Hydrogr. Z. Suppl.* 12 (A8), 1-95, 1973.

[9] Hasselmann, K.and Collins, J.I., Spectral dissipation of finite-depth gravity waves due to turbulent bottom friction. *J. Mar. Res.* 26, 1-12, 1968.

[10] Hasselmann, K. and Hasselmann, S., On the nonlinear mapping of an ocean wave spectrum into a synthetic aperture radar image spectrum and its inversion, *J. Geophys. Res., 96*, C6, 10713, 1991.

[11] Hersbach, H., Application of the adjoint of the WAM modeltop inverse wave modeling, *J. Geophys. Res., 103*, 10,469, 1998.

[12] Krogstad, H.E., A simple derivation of Hasselmann's nonlinear ocean-to-synthetic aperture radar transform, *J. Geophys. Res., 97*, C2, 2421, 1992.

[13] Lyzenga, D.R., Unconstrained inversion of waveheight spectra from SAR images. *Trans. Geosci. Remote Sens.*, 40, 261, 2002.

[14] Le Dimet, F.-X. and O. Talagrand, Variational algorithms for analysis and assimilation of meteorological observations: Theoretical aspects. *Tellus, 38A*, 97, 1986.

[15] Madsen, O.S., Poon, Y.-K. and Graber, H.C. Spectral wave attenuation by bottom friction: Theory. *Proc. 21st ICCE,*1988.

[16] Polak, E. *Computational Methods in Optimization* Academic Press, §2.3, 1971.

[17] Ris, R.C., N. Booij, and L.H. Holthuijsen, *SWAN Cycle 1 User Manual,* Department of Civil Engineering, Delft University of Technology, 1995.

[18] Ris, R.C., L.H. Holthuijsen and N. Booij, A third-generation wave model for coastal regions: 2. Verification. *J. Geophys. Res., 104*, 7667, 1999

[19] Talagrand, O. and P. Courtier, Variational assimilation of meteorological observations with the adjoint vorticity equation: I. Theory. *Q. J. R. Meteorol. Soc., 113*, 1311, 1987

[20] Weber, S.L., Eddy viscosity and drag-law models for random ocean-wave dissipation. *J. Fluid Mech.* 232, 73-98,1991.